EXPERIMENTS IN TURBULENT SOAP-FILM FLOWS: MARANGONI SHOCKS, FRICTIONAL DRAG, AND ENERGY SPECTRA

BY

TUAN ANH TRAN

DISSERTATION

Submitted in partial fulfillment of the requirements
for the degree of Doctor of Philosophy in Mechanical Engineering and Science
in the Graduate College of the
University of Illinois at Urbana-Champaign, 2010

Urbana, Illinois

Doctoral Committee:

Associate Professor Gustavo Gioia, Chair
Professor Nigel Goldenfeld
Associate Professor Kenneth Christensen
Associate Professor Jonathan Freund

Abstract

We carry out unprecedented experimental measurements of the frictional drag in turbulent soap-film flows over smooth walls. These flows are effectively two-dimensional, and we are able to create soap-film flows with the two types of turbulent spectrum that are theoretically possible in two dimensions: the “enstrophy cascade,” for which the spectral exponent $\alpha = 3$, and the “inverse energy cascade,” for which the spectral exponent $\alpha = 5/3$. We find that the functional relation between the frictional drag f and the Reynolds number Re depends on the spectral exponent: where $\alpha = 3$, $f \propto \mathrm{Re}^{-1/2}$; where $\alpha = 5/3$, $f \propto \mathrm{Re}^{-1/4}$.

These findings cannot be reconciled with the classic theory of the frictional drag. The classic theory provides no means of distinguishing between one type of turbulent spectrum and another, and cannot account for the existence of a “spectral link” between the frictional drag and the turbulent spectrum. In view of our experimental results, we conclude that the classic theory must be considered incomplete.

In contrast, our findings are consistent with a recently proposed spectral theory of the frictional drag. In this theory the frictional drag of turbulent flows on smooth walls is predicted to be $f \propto \mathrm{Re}^{(1-\alpha)/(1+\alpha)}$, where α is the spectral exponent. This prediction is in exact accord with our experiments on soap-film flows. It is also in accord with the available experimental data on three-dimensional pipe flows, where a single type of spectrum is possible: the “energy cascade,” for which $\alpha = 5/3$ (the same as for the inverse energy cascade). In fact, for $\alpha = 5/3$ the prediction of the spectral theory coincides with the emprirical law of Blasius ($f \propto \mathrm{Re}^{-1/4}$), which gives the best representation of the available experimental results for three-dimensional pipe flows of moderate turbulent strength (starting from $\mathrm{Re} \approx 2,500$ and up to $\mathrm{Re} \approx 100,000$).

In carrying out our experiments on the frictional drag, we discover the spontaneous occurrence in unobstructed soap-film flows of a type of shock related to the elasticity of the film. By means of extensive experimental measurements, we verify that these shocks are dissipative and diffusive; that they give rise to fluctuations independently from the boundaries, with a strong but circumscribed effect on the spatial distribution of turbulent intensity; and that they alter the structure of the turbulent spectrum downstream from the shock.

We show that a simple one–dimensional model is capable of capturing the most salient features of our experimental measurements and observations on the shocks. In this model the steady-state equation of momentum balance contains four terms: the inertial force, the elastic force, the gravitational force, and the drag force of the ambient air. The elastic force consists of the gradient of the surface tension, and it can be computed under the assumption (which is satisfied in our experiments) that the film is in the Marangoni regime, i.e., that as the flow moves through the shock there is no time for diffusional exchange of soap molecules between the bulk and the faces of the film, so that the concentration of soap molecules in the bulk of the film remains invariant.

To my Family

Acknowledgments

I would like to express my gratitude to the following individuals who have helped me make this thesis possible.

First and foremost, I would like to thank my advisor, Professor Gustavo Gioia, for his strong and unwavering support throughout the course of my doctoral work. His passion and high standard for science has always given me an extra push to achieve better results. By working with him, I have learned that any challenge could be overcome with determination and hard work. His ability of communicating scientific results in a simple, clear, and elegant manner is an inspiration for me.

I also wish to thank Professor Nigel Goldenfeld, for his encouragement and valuable guidance. He has helped me in keeping pace with my graduate career and introduced me to many people within the discipline. More importantly, my confidence was considerably strengthened due to his faith in my work.

In the last two years of my Ph.D., I was very fortunate to work in the laboratory of Professor Walter Goldburg at the University of Pittsburgh. I am grateful to him for being not only my teacher but also my friend. I still remember how he patiently taught me every little detail of experimental physics, and how he patiently listened to my random and sometimes chaotic ideas. Our lunches together frequently ended up with his hands covered with chalk as he tried to explain some ideas of physics to me. His extraordinary enthusiasm for physics has inspired and enriched my growth as a researcher.

I am grateful to Professor Hamid Kellay (University of Bordeaux) for his gracious help and guidance with many aspects of my experiments. His mastery in tweaking soap films was

of immense help during the course of my research.

I would like to thank Professor Kenneth Christensen and Professor Jonathan Freund for agreeing to be on my thesis committee and reviewing my thesis. In particular, I am grateful to Professor Christensen for generously lending us equipments from his laboratory.

I am also indebted to Professor Anne Robertson, for whom I worked for a semester as a teaching assistant at the University of Pittsburgh.

Pinaki Chakraborty has had an important role in my graduate years. Beside being a friend, he is also my mentor. His patience in teaching me physics and his constant stream of new ideas were very helpful in my graduate career.

I would like to thank my many friends at University of Illinois, particularly Steve Holman, Carlo Zuniga Zamalloa, Ricardo Mejia Alvarez, Nicholas Guttenburg, and Paulo Zandonade, for making the years of my graduate career extremely joyful. I will miss the late night times we struggled with homework and rewarded ourselves with pizzas at wee hours in the morning. A special thank goes to Kuan-Khoon Tjan and Tapan Sabuwala for helping me improve my English and joining me in running the Chicago Marathon. Kuan-Khoon and Tapan shared an office with me and I enormously benefited from my conversations with them, both personally and scientifically. They were my wonderful sources of advice of almost everything, from how to rent a car at a discount, to what is the fastest way to learn *Numerical Recipes in C*.

I am grateful to have many good friends in Professor Goldburg's lab at University of Pittsburgh. In particular, I am indebted to Ildoo Kim, Jason Larkin, Alisia Prescott, Rory Cerbus, Stefanus, and Christina McDonald for helping me with the experimental work. Their friendship made my time in Pittsburgh enjoyable.

Most importantly, I would never have enough strength and patience to finish this work without the unconditional love of my family. My parents and my younger brother, to all of whom this thesis is dedicated to, have been my endless source of cherish, comfort, and support, even though they are halfway around the world. I would also like to thank my significant other, Na Van, for her love and faithful support during the final stage of my

Ph.D.

Finally, I gratefully acknowledge the Vietnam Education Foundation (VEF) for providing me with the opportunity to pursue a Ph.D. degree in the United States. In particular, I would like to extend my sincere thanks to “anh” Kien Pham and Lynn McNamara, whose tireless effort made VEF and its mission possible. The work presented in this thesis was also partly supported by the National Science Foundation under grant No. NSF DMR 06-04435.

Table of Contents

List of Figures

Chapter 1

Introduction

There is a missing "spectral link" in turbulence. Much is known about the macroscopic properties of turbulent flows—the properties of interest in engineering, such as the mean velocity profile of a pipe flow [3, 4, 5]. And much is known about the turbulent spectrum—the statistics of the fluctuations in the flow [6, 7, 8]. Yet there exists no link between the macroscopic properties and the spectrum, and these have remained the subjects of split research efforts and disconnected book chapters.

Consider, for example, what is perhaps the most important macroscopic property of a turbulent flow past a wall: the frictional drag. The frictional drag sets the cost of pumping oil through a pipeline, the draining capacity of a river in flood, and other quantities of engineering interest [3, 4, 5, 9, 10]. It is defined as the dimensionless ratio $f = \tau/\rho U^2$, where τ is the shear stress or force per unit area that develops between the flow and the wall, ρ is the density of the fluid, and U is the mean velocity of the flow. Already in XVIII Century France, f was the subject of large-scale experiments performed in connection with the design of a waterworks for the city of Paris [11, 12]. The celebrated theory [4, 5] of the frictional drag was formulated eighty years ago by Ludwig Prandtl, the founder of turbulent hydraulics. Numerous variants [5, 13, 14, 15, 16, 17, 18, 19, 20, 21] of Prandtl's theory have since been proposed. Yet Prandtl's theory and all of its variants have been predicated on dimensional analysis and similarity assumptions, without reference to the spectral structure of the turbulent fluctuations. If there be a spectral link, these theories are blind to it.

To grasp the possible practical implications of the existence of a spectral link, consider, for example, the well-known drag-lessening effect of polymeric additives in oil pipelines (where polymeric additives are customarily used to reduce the cost of pumping) [22, 23]. Many theories have been proposed to explain the drag-lessening effect. None of these theories has been accepted widely, and none takes into account the crucial fact that polymeric additives change the spectral exponent [24]. By virtue of the spectral link, a change in spectral exponent should be accompanied by a change in the frictional drag. Thus, the spectral link may provide the key to understanding the drag-lessening effect of polymeric additives. It may also provide the key to understanding the poorly known, drag-altering effects of other agents which also change the spectral exponent, for example particulate suspensions (found in rivers in flood) and entrained bubbles [25] (found in water-treatment plants). If the existence of a spectral link can be confirmed experimentally, we will no longer have to carry out complex, expensive tests to ascertain the frictional drag in flows with polymeric additives, particulate suspensions, or entrained bubbles. Instead we will be able to predict the frictional drag from simple, inexpensive measurements of the turbulent spectrum.

Here we are concerned with a recently proposed spectral theory of the frictional drag [1, 26]. According to this theory, the mathematical relation among the frictional drag in a turbulent pipe or channel flow, the Reynolds number of the flow, and the roughness of the pipe or channel is set by the spectral exponent. The theory has been used to predict a number of long–unexplained features in the classsical experimental data set of Nikuradse [1]; to show that the empirical exponents of Blasius, Strickler, and Manning are but recast forms of the spectral exponent of Kolmogorov [26]; to predict the frictional drag associated with a general spectral exponent α [27]; to ascertain the existence of fully developed turbulence on the basis of experimental data on the frictional drag [28]; to infer the value of the intermittency exponent on the basis of the experimental data on the frictional drag [28, 29]; to help interpret experimental data on the frictional drag in commercially–rough pipe flows [15]; to predict the frictional drag in flows with the Heisenberg spectrum [30]; and to formulate a model of scouring of granular beds by turbulent cauldrons [31, 32].

For smooth-walled pipes, the theory can be used to make the prediction, $f \sim \mathrm{Re}^{(1-\alpha)/(1+\alpha)}$, where Re is the Reynolds number and α is the spectral exponent [27]. Our main objective here is to test this prediction of the spectral theory. To achieve our objective, we carry out experiments in turbulent soap-film flows. Turbulent soap-film flows may be thought of as two-dimensional counterparts of turbulent pipe flows [33, 34, 35, 36]. There have never been experimental measurements of the frictional drag in soap-film flows.

Soap-film flows are particularly suitable to test the spectral theory, because in these flows the spectral exponent can take either of two values, $\alpha = 3$ (enstrophy cascade) or $\alpha = 5/3$ (inverse energy cascade),—at least in theory [34, 35, 37, 38, 39]. (α can take but a single value in most three-dimensional flows [7, 8].) In practice, soap-films flows with $\alpha = 3$ are relatively easy to realize [33], but to the best of our knowledge we are the first to have realized a soap-film flow with $\alpha = 5/3$.

In the course of measuring the frictional drag of soap-film flows, we discovered a new type of shock associated with the elasticity of the film. In Chapter 2 we discuss our theoretical and experimental work [40] on "Marangoni Shocks."

In Chapter 3 we review the spectral theory of the frictional drag. In Chapter 4, we turn to the experimental test [41] of the prediction of the theory for smooth–walled soap-film flows, and discuss our measurements of the frictional drag and the accompanying turbulent spectra. We also discuss the method whereby we were able to obtain soap-film flows of spectral exponent $\alpha = 5/3$ (inverse energy cascade).

A soap-film channel constitutes the primary element of our experimental setup and we have introduced a number of improvements in its design. We discuss these improvements and other experimental details in Chapter 5. Lastly, in Chapter 6 we make concluding remarks and outline directions for future research.

Chapter 2

Marangoni shocks in unobstructed soap-film flows

It is widely thought that in steady, gravity-driven, unobstructed soap-film flows, the velocity increases monotonically downstream. In this chapter* we show experimentally that the velocity increases, peaks, drops abruptly, then lessens gradually downstream. We argue theoretically and verify experimentally that the abrupt drop in velocity corresponds to a Marangoni shock, a type of shock related to the elasticity of the film. Marangoni shocks induce locally intense turbulent fluctuations and may help elucidate the mechanisms that produce two-dimensional turbulence away from boundaries.

2.1 Introduction and experimental setup

Soap-film flows [42, 43, 36, 34] have long been used to study two-dimensional (2D) turbulence, a type of turbulence that differs from its three-dimensional (3D) counterpart in crucial respects. For example, in 3D turbulence the energy may cascade only from larger to smaller lengthscales whereas in 2D turbulence the energy may cascade in either direction [37, 38, 39]. Disparate directions of energy transfer result in disparate apportionings of the turbulent kinetic energy among the lengthscales of the flow [37, 38, 39]. Besides the theoretical interest inherent in its distinctive characteristics, 2D turbulence is relevant to the large-scale irregularities encountered in 2D atmospheric flows—flows that are confined to two dimensions by geostrophic forces and a stratified atmosphere [44, 34]. Examples of large-scale irregularities in 2D atmospheric flows include hurricanes, typhoons, and the Great Red Spot of Jupiter

---

*Part of the work described in this chapter has been published in [40]

[45, 46, 47, 48, 49].

In the typical experimental setup used to study soap-film flows [50], a film hangs between two long, vertical, mutually parallel wires a few centimeters apart from one another. The film drains into a reservoir at the bottom of the setup and draws a soapy solution from a reservoir at the top. Driven by gravity, a steady vertical flow soon becomes established within the film (Fig. 2.1). Then, the thickness h of the film is roughly uniform on any cross section of the flow [51], and we write $h = h(x)$, where x is an axis that runs vertically along the centerline of the flow (Fig. 2.1). In a typical flow $h \approx 10\,\mu\text{m}$, much smaller than both the width w and the length L of the flow (Fig. 2.1). As a result, the velocity of the flow lies on the plane of the film, and the flow is 2D. Since the viscous stresses (and the attendant velocity gradients) are confined to narrow layers adjacent to the wires, the mean (time-averaged) velocity u is roughly uniform on any cross section of the film [52], and we write $u = u(x)$. Thus, assuming that the soapy solution is incompressible, the product $h(x)u(x)$ equals the flux q per unit width of film and is independent of x for a steady flow.

Analyses of steady flows have accounted for the gravitational force (i.e., the driving force), the inertial force, the drag force of the ambient air, and the drag force of the wires. Rutgers et al. [52] have shown that the drag force of the wires is negligible as compared to the drag force of the ambient air and may be dropped from the equation of momentum balance, so that the steady state represents a state of dynamic equilibrium among the inertial force, the gravitational force, and the drag force of the ambient air. Then, a prediction can be made that in a steady flow the mean velocity is a monotonically increasing function of x and approaches a terminal velocity asymptotically downstream [51, 52]. This prediction has not been tested, but it is thought to be in qualitative agreement with the few known experiments [51, 52]. In contrast to this prediction, in our experiments the mean velocity is a strongly non-monotonic function of x.

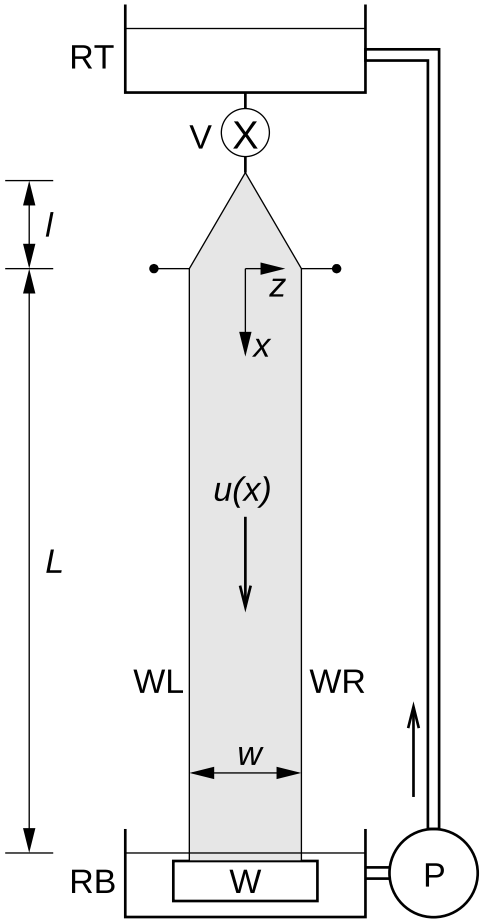

Figure 2.1: Typical experimental setup used to study steady, gravity-driven, unobstructed soap-film flows. Axis x runs vertically along the centerline of the flow. Wires WL and WR are thin nylon-fishing lines kept taut by weight W. The film hangs from the wires; its width increases from 0 to w over an expansion section of length l, then remains constant and equal to w over a measurement section of length $L \gg l$. (The origin of x is at the top of the measurement section. L is the "length of the flow" and w the "width of the flow.") Reservoir RT contains a soapy solution which flows through valve V and into the film. After flowing through the film with mean velocity $u(x)$, the soapy solution drains into reservoir RB and returns to reservoir RT via pump P. In our experiments, the soapy solution consists of $\simeq 2.5\,\%$ Dawn Nonultra in water and it is seeded with small particles (diameter $\approx 1\,\mu$m) to scatter light for LDV measurements; $w = 2.5$ to $5.1\,$cm; $L = 1.05$ to $1.39\,$m; and $l = 23.5\,$cm.

2.2 Experimental results

To measure the mean velocity u, we use Laser Doppler Velocimetry (LDV). In Fig. 2.2 we show plots of our measurements of u along the centerline of several representative flows. In each flow, u increases downstream up to a certain point whereupon it peaks, drops abruptly to a fraction of its peak value, then continues to lessen gradually downstream.

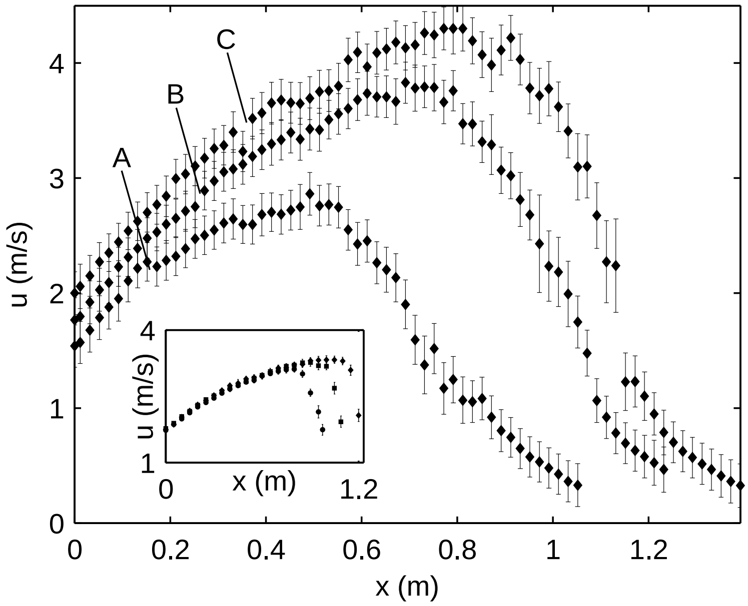

Figure 2.2: Plots of the mean velocity u vs. x for three steady flows. The width $w = 5.1\,\mathrm{cm}$ for all flows; both the length L and the flux per unit width q change from flow to flow. $L = 1.05\,\mathrm{m}$ and $q = 3.8\,10^{-6}\,\mathrm{m}^2/\mathrm{s}$ (A), $L = 1.23\,\mathrm{m}$ and $q = 4.9\,10^{-6}\,\mathrm{m}^2/\mathrm{s}$ (B), $L = 1.39\,\mathrm{m}$ and $q = 5.5\,10^{-6}\,\mathrm{m}^2/\mathrm{s}$ (C). Inset: Plots of u vs. x for three steady flows. $w = 5.1\,\mathrm{cm}$ and $q = 5.7\,10^{-6}\,\mathrm{m}^2/\mathrm{s}$ for all flows; L changes from flow to flow.

From the incompressibility condition ($uh = q$, where h is the thickness of the film and q the flux per unit width of film), we expect that the abrupt drop in u should be accompanied by an abrupt increase in h. To verify the presence of this abrupt increase in h, we light a face of a film with the monochromatic radiation of sodium lamp and observe the interference fringes that form on the face of the film. (The thickness of the film is constant along a fringe; it differs by a fraction of the wavelength of the light, or a fraction of a μm, between any two successive fringes.) In Fig. 2.3a we show a photograph of the interference fringes on the part of a film where u drops abruptly. The distance between any two successive fringes decreases rapidly in the downstream direction, signaling an abrupt increase in h. The film thickens so much that the fringes become blurred and cannot be counted.

To verify the presence of an abrupt increase in h by means of an alternative technique, we put Flourescein dye in the soapy solution and focus incoherent blue light on a spot on the film. The spot becomes fluorescent, and we monitor the intensity of the fluorescence using a photodetector whose counting rate is proportional to h. In Fig. 2.3b we show plots of these measurements of h along four cross sections of a flow. These cross sections lie on the part of the flow where u drops abruptly. The thickness trebles over a short distance of a few centimeters in the downstream direction.

2.3 Theory

To explain our experimental results, we write the steady-state equation of momentum balance in the form

$$\rho h u u_x = 2\sigma_x + \rho g h - 2\tau_a, \tag{2.1}$$

where ρ is the density, $(\cdot)_x = d(\cdot)/dx$, σ is the surface tension, g is the gravitational acceleration, and τ_a is the shear stress due to air friction. From left to right, the terms in (2.1) represent the inertial force, the elastic force, the gravitational force, and the drag force of the ambient air. (Please refer to appendix A.1 for further discussion.) Here we follow Rutgers et al. [52] and use (as a rough approximation)

$$\tau_a = 0.3\sqrt{\rho_a \mu_a u^3/(x+l)}, \tag{2.2}$$

the Blasius expression for the shear stress on a rigid plate that moves at a constant velocity u through air of density $\rho_a = 1.2\,\mathrm{kg/m^3}$ and viscosity $\mu_a = 1.7 \times 10^{-5}\,\mathrm{kg/ms}$. (Please refer to appendix A.3 for further discussion.)

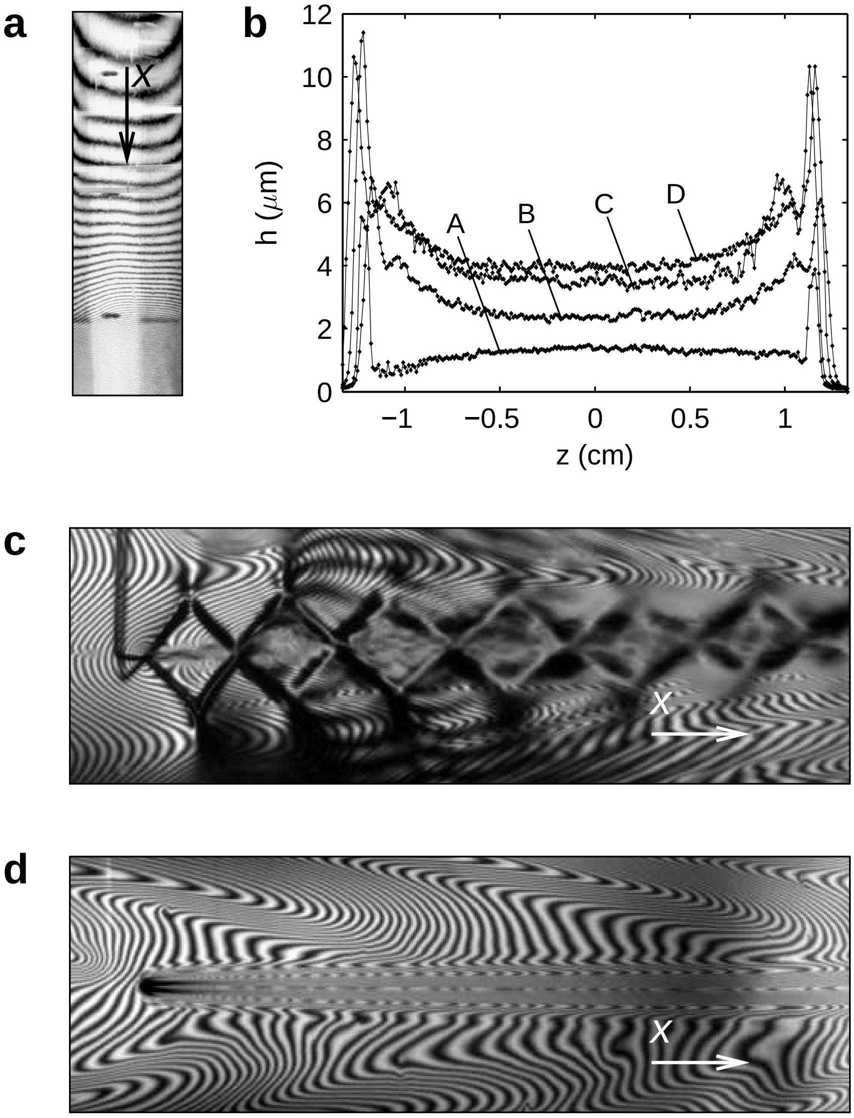

Figure 2.3: **(a)** Fringes over the part of a film where the velocity drops abruptly. **(b)** Plots of the thickness vs. z along four cross sections of a flow of width 2.5 cm and length 1.2 m. The cross sections are at $x = 0.95\,\mathrm{m}$ (A), $x = 1.04\,\mathrm{m}$ (B), $x = 1.05\,\mathrm{m}$ (C), and $x = 1.07\,\mathrm{m}$ (D). The large peaks near the lateral edges of each cross section are due to backscattering from the wires. Fringes at a piercing upstream **(c)** and downstream **(d)** of the drop in velocity; fields of view = $5\,\mathrm{cm}\times 1\,\mathrm{cm}$.

To obtain an expression for σ_x, we argue that the concentration of soap molecules in the bulk of the film remains constant in our experiments, because there is no time for diffusional exchange between the bulk and the faces of the film [2, 53]. We start by noting that a change in h (and the attendant stretching of the film) may disturb the mutual equilibrium between the bulk and the faces of the film. To show that the concentration of soap molecules in the bulk remains constant, we must show that the rate of change of h does not allow time for soap molecules to diffuse between the bulk and the faces of the film, so that t_D (the timescale of diffusion) $\geq t_d$ (the timescale associated with changes in h).

For $h = 10\,\mu$m (a typical value in our experiments) we estimate $t_D = 1\,$s [2]. To obtain an upper bound on t_d, we argue that t_r (the residence time of a drop of soapy solution in the flow) $\gg t_d$. For $u = 1\,$m/s and $L = 1\,$m (typical values in our experiments) we estimate $t_r = L/u = 1\,$s, and conclude that $t_D \approx t_r \gg t_d$, as we expected. Thus, there is no time for diffusional exchange between the bulk and the faces of the film, and the concentration of soap molecules in the bulk of the film remains constant in our experiments. Where the concentration of soap molecules in the bulk of the film remains constant, the film is said to be in the *Marangoni regime* (see Appendix A.2).

Now, the surface tension of a dilute soap solution can be expressed as $\sigma = \sigma_0 - RT\Gamma$, where σ_0 is the surface tension of pure water, R is the gas constant, T is the absolute temperature, and Γ is the concentration of soap molecules on the faces of the film [2]. By definition, $\Gamma = (c - c_b)h/2$, where c is the overall concentration of soap molecules in the film and c_b is the concentration of soap molecules in the bulk of the film. Since c remains constant (because of incompressibility) and c_b also remains constant (because the film is in the Marangoni regime), it follows that $\Gamma_x = (c - c_b)h_x/2$ and $\sigma_x = -\rho U_M^2 h_x/2$. Here $U_M \equiv \sqrt{RT(c - c_b)/\rho}$ is the *Marangoni speed*—a constant, independent of h, that quantifies the speed at which disturbances in h travel on the plane of the film [2, 53]). (Please refer to appendix A.2 for further discussion.) By substituting $2\sigma_x = -\rho U_M^2 h_x$ and $h = q/u$ in (2.1), we obtain the governing equation

$$u_x = u\frac{g - 2\tau_a u/\rho q}{u^2 - U_M^2}. \tag{2.3}$$

2.4 Analysis and further experiments

In (2.3) we can distinguish two types of flow: a supercritical flow in which $u > U_M$ and $u_x > 0$, and a subcritical flow in which $u < U_M$ and $u_x < 0$. We conjecture that in our experiments the flow is supercritical upstream of the drop in velocity and subcritical downstream. Consistent with this conjecture, for any fixed q the flow upstream of the drop in velocity remains invariant to changes in the length of the flow (inset of Fig. 2.2).

To confirm that flows are supercritical upstream of the drop in velocity and subcritical downstream, we use pins to pierce a flow upstream and downstream of the drop in velocity (Figs. 2.3c and d, respectively). Upstream of the drop in velocity the Mach angle $\approx 50^o$ (from Fig. 2.3c), and the local $u = 1.83\,\mathrm{m/s}$ (from an LDV measurement); thus $U_M \approx \sin 50^o \times 1.83\,\mathrm{m/s} = 1.4\,\mathrm{m/s}$ in our experiments.

Let us test the governing equation (2.3) for one of our experiments. We adopt a value of U_M and a value of q and perform two computations. First, we integrate equation (2.3)) downstream from $x = w$ with boundary condition $u(w) = u_w$, where u_w is the velocity measured at $x = w$ in the experiment. (We integrate downstream from $x = w$ to avoid any end effects that might have been present in the experiment close to $x = 0$.) This first computation gives a function $u(x)$ that should fit the experiment upstream of the drop in velocity.

Second, in an analogous way to the first computation, we integrate Equation (2.3) upstream from $x = L - w$ with boundary condition $u(L - w) = u_{L-w}$, where u_{L-w} is the velocity measured at $x = L - w$ in the same experiment. This second computation gives a function $u(x)$ that should fit the experiment downstream of the drop in velocity.

We perform the same computations for each one of our experiments trying different values of q and U_M, and choose the *optimal values of* q and the *optimal value of* U_M—that is to say, the values of q (one for each experiment) and the value of U_M (the same for all experiments) that yield the best fits to the experiments (Fig. 2.4). The optimal value of U_M, 1.48 m/s, is in remarkable agreement (for a simple one-dimensional model) with our estimate from Fig. 2.3c (1.4 m/s).

The optimal values of q are in reasonable agreement with the experimental estimates for q. (caption to Fig. 2.4). We estimate these values of q by measuring the volume of soapy solution that drains into reservoir RB (Fig. 2.1) in a given time interval and divide this volume by w.

We conclude that a drop in velocity signals a supercritical-to-subcritical transition and corresponds to a *Marangoni shock*. In theory the drop in velocity is infinitely steep and may be said to take place at $x = x^*$, where u attains the value of U_M (and u_x becomes singular) in the subcritical flow (Fig. 2.4). But in experiments the drop in velocity takes place over a finite span Δx whose magnitude appears to increase monotonically with q (Fig. 2.4) and whose downstream edge is located at about $x = x^*$, the theoretical position of the shock (a position which appears to move downstream as q increases). Thus in our simple theory the shock is sharp whereas in experiments the shock is diffused over a finite span Δx.

To understand this discrepancy, consider the energetics of a shock. It can be shown theoretically that a shock must dissipate energy at a steady rate. In fact, the energy per unit area on the plane of the film is the sum of the elastic, kinetic, and potential energy, $e = 2\sigma + \rho h u^2/2 - \rho g h x$. Thus the energy conveyed per unit time and unit width of film is eu, and the shock must dissipate a power per unit width $P = -[\![eu]\!]$, where $[\![(\cdot)]\!] \equiv (\cdot)_+ - (\cdot)_-$, the subscript "+" stands for "downstream of the shock" and the subscript "−" stands for "upstream of the shock." By substituting $\sigma = \sigma_0 - \rho U_M^2 h/2$ and $h = q/u$, we obtain $P = -2\sigma_0[\![u]\!] - \rho q[\![u^2]\!]/2 > 0$. Thus the shock must dissipate energy at a steady rate, as we anticipated.

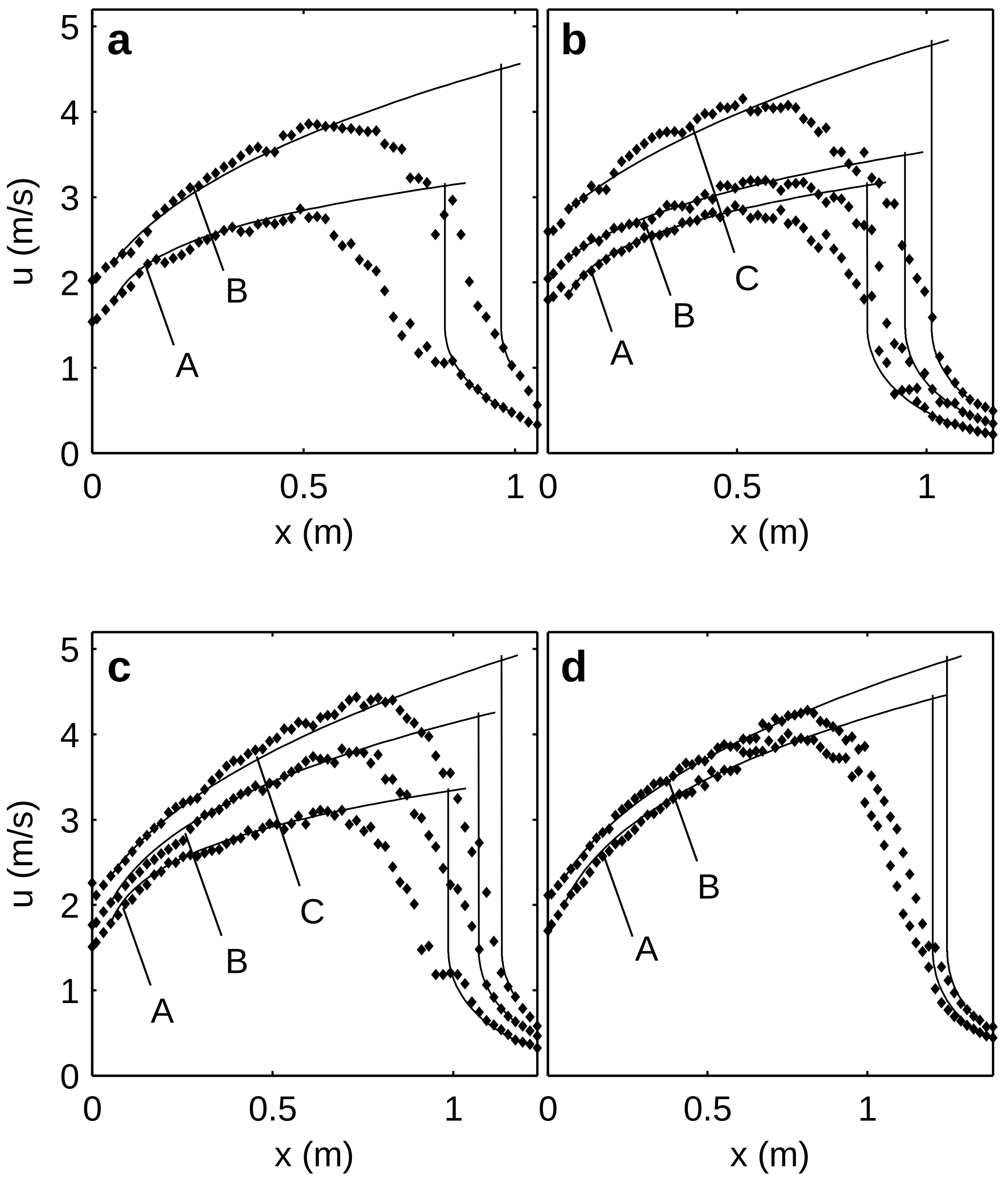

Figure 2.4: Plots of the computational $u(x)$ (lines) and experimental $u(x)$ (points) for ten different flows. The computations are for $U_M = 1.48\,\mathrm{m/s}$ and the values of q indicated below (the experimental estimates for q are indicated in parentheses). $w = 5.1\,\mathrm{cm}$ for all flows. **(a)** Flows of length 1.05 m: (A) $q = 5.7\,10^{-6}\,\mathrm{m^2/s}$ ($3.9\,10^{-6}\,\mathrm{m^2/s}$), (B) $25\,10^{-6}\,\mathrm{m^2/s}$ ($5.7\,10^{-6}\,\mathrm{m^2/s}$); **(b)** flows of length 1.17 m: (A) $5.7\,10^{-6}\,\mathrm{m^2/s}$ ($5.1\,10^{-6}\,\mathrm{m^2/s}$), (B) $7.4\,10^{-6}\,\mathrm{m^2/s}$ ($5.9\,10^{-6}\,\mathrm{m^2/s}$), (C) $30\,10^{-6}\,\mathrm{m^2/s}$ ($7.5\,10^{-6}\,\mathrm{m^2/s}$); **(c)** flows of length 1.23 m: (A) $6.1\,10^{-6}\,\mathrm{m^2/s}$ ($4.1\,10^{-6}\,\mathrm{m^2/s}$), (B) $14\,10^{-6}\,\mathrm{m^2/s}$ ($5.3\,10^{-6}\,\mathrm{m^2/s}$), (C) $31\,10^{-6}\,\mathrm{m^2/s}$ ($6.5\,10^{-6}\,\mathrm{m^2/s}$); and **(d)** flows of length 1.39 m: (A) $16\,10^{-6}\,\mathrm{m^2/s}$ ($4.7\,10^{-6}\,\mathrm{m^2/s}$), (B) $25\,10^{-6}\,\mathrm{m^2/s}$ ($6.3\,10^{-6}\,\mathrm{m^2/s}$).

We argue (i) that the shock dissipates energy by powering locally intense turbulent fluctuations and (ii) that these fluctuations must extend roughly over the same span Δx as the shock that powers them. (An analogy with turbulent hydraulic jumps in open channels supports these arguments [54, 55].)

To test these arguments we use LDV to measure the mean velocity u and the root-mean-square velocity u_{rms} along the centerline of a representative flow (Fig. 2.5). From a comparison of Figs. 2.5a and b, we confirm that the shock is accompanied over its entire span Δx by velocity fluctuations that are up to thrice as intense as the velocity fluctuations that prevail both upstream and dowstream of Δx. We conjecture that intense velocity fluctuations can arise more readily where the mean velocity is higher; this may explain why the locally intense velocity fluctuations—and the diffusive shock that powers them—are located on the supercritical side of the theoretical position of the shock.

To verify that the velocity fluctuations are turbulent, we obtain the energy spectrum on the centerline of the flow for three cross sections: one upstream, one within, and one downstream of the shock (inset to Fig. 2.5b). (These cross sections are marked "A," "B," and "C" in Fig. 2.5b.) The area under the spectrum is larger for cross section B (within the shock) than for each of the other two cross sections A and C, confirming that the turbulence is more intense within the shock than elsewhere in the flow. Further, the slope of the spectrum at intermediate wavenumbers and the shape of the spectrum at low wavenumbers differ on either side of the shock, indicating that the spectrum undergoes structural changes as the flow traverses the shock.

2.5 Conclusions

We have demonstrated the spontaneous occurrence of Marangoni shocks in the steady, gravity-driven, unobstructed soap-film flows that are customarily used in experimental work on two-dimensional turbulence. By means of extensive experimental measurements, we have

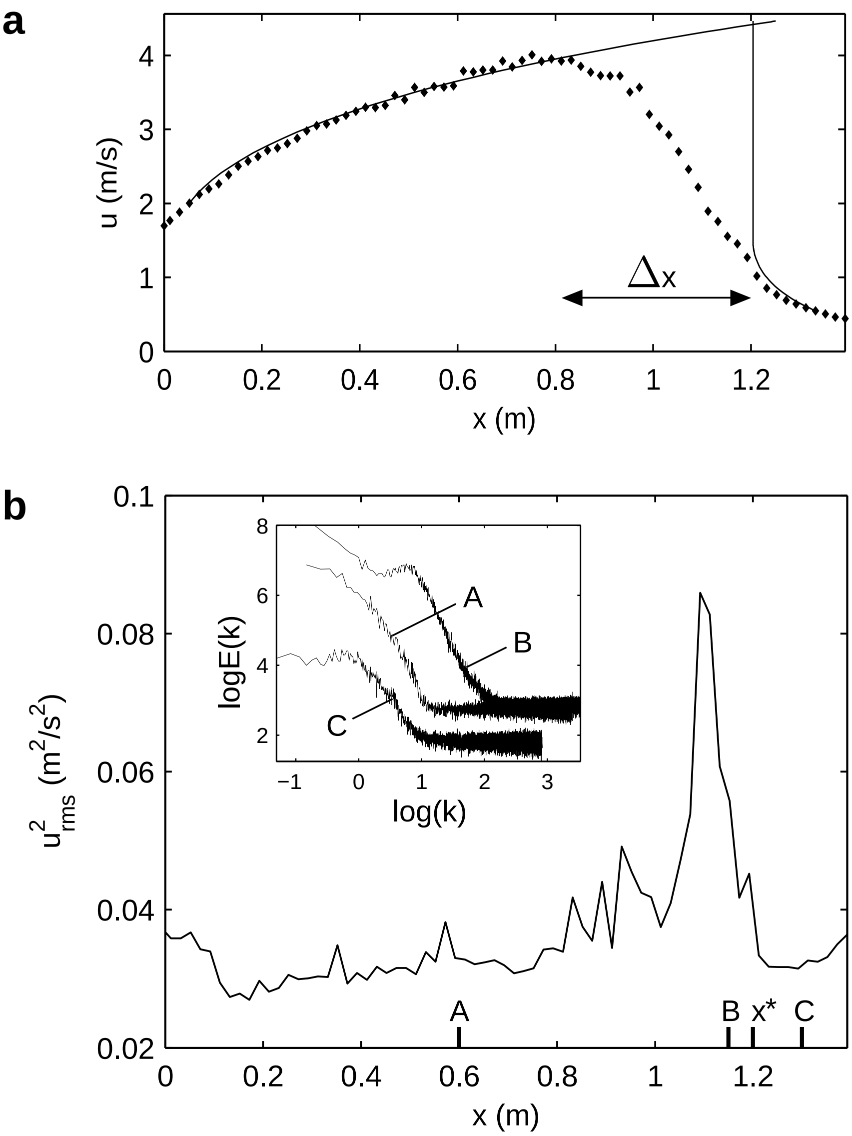

Figure 2.5: **(a)** Plots of the computational $u(x)$ (lines) and the experimental $u(x)$ (points) for a representative flow. Δx is the span of the shock. **(b)** Plot of the experimental u^2_{rms} (an index of the energetic contents of the velocity fluctuations) vs. x for the same flow. Inset: energy spectra at the centerline of the same flow for the cross section at $x = 0.60\,\text{m}$ (A), $x = 1.17\,\text{m}$ (B), and $x = 1.30\,\text{m}$ (C). These are the cross sections marked "A," "B," and "C" in part **b**. The spectra are log-log plots of the energy density E (m^3/s^2) vs. the wavenumber k (1/m).

shown that these shocks are dissipative and diffusive; that they give rise to fluctuations independently from the boundaries, with a strong but circumscribed effect on the spatial distribution of turbulent intensity; and that they alter the structure of the turbulent spectrum downstream from the shock.

We have also shown that a simple one–dimensional model is capable of capturing the most salient features of our experimental measuremets and observations on the shocks. In this model the steady-state equation of momentum balance contains four terms: the inertial force, the elastic force, the gravitational force, and the drag force of the ambient air. The elastic force consists of the gradient of the surface tension, and it can be computed under the assumption (which was satisfied in our experiments) that the film is in the Marangoni regime, i.e., that as the flow moves through the shock there is no time for diffusional exchange between the bulk and the faces of the film, so that the concentration of soap molecules in the bulk of the film remains invariant.

We conclude that the presence of shocks should be factored in in the interpretation of experimental measurements, and submit that shocks may furnish a convenient setting to study localized turbulence production in two dimensions.

Chapter 3

Spectral theory of the frictional drag

A spectral link between the frictional drag and the turbulent spectrum has been recently established by Gioia and Chakraborty. The spectral link consists of a model by which the frictional drag can be computed from a knowledge of the turbulent spectrum [1, 26]. In this model the shear stress at the wall arises from the transfer of momentum effected by the eddies of the turbulent flow, where the capacity of an eddy to transfer momentum is set by the revolving velocity of the eddy. Thus the physical basis for the model is momentum transfer, and the key assumption of the model is that the revolving velocity of a turbulent eddy of any given size can be determined from the turbulent spectrum.

This chapter is devoted to a review of the spectral theory of the frictional drag. The emphasis is on some of the predictions of the theory for 3D turbulent flows (where only one type of spectrum is possible, the energy cascade) and some of the predictions of the spectral theory for 2D turbulent flows (where two types of spectrum are possible, the inverse energy cascade and the enstrophy cascade). The predictions for 2D turbulent flows will be the subject of the following chapter, in which we will test the predictions experimentally, in soap-film flows.

We start the chapter with a brief review of the concept of the frictional drag and the classical experimental data set on the frictional drag in pipe flows.

3.1 Frictional drag in turbulent flows

Turbulent flows are characterized by turbulent fluctuations (or eddies) that span a wide range of length and time scales. Even though the Navier–Stokes equations [56, 57] that describe the flow have been known since the XIX Century, our understanding of turbulence remains far from complete. One of the most important problems in science and engineering that involves turbulence is to predict accurately the frictional drag experienced by a turbulent flow past a wall. The frictional drag is typically represented in dimensionless form as $f \equiv \tau/\rho U^2$, where τ is the shear stress (or frictional force per unit area) that develops between the flow and the wall, ρ is the fluid density, and U is the mean velocity of the flow.

Because of its importance in common applications, much research has been carried out on the frictional drag. Already in XVIII Century France, the frictional drag was the subject of large-scale experiments performed in connection with the design of a waterworks for the city of Paris [11, 12]. In 1883, it was predicted [58], and subsequently confirmed by numerous experiments, that in smooth-walled pipe flows the frictional drag f depends on the Reynolds number, i.e., on the dimensionless ratio between the inertial forces and the viscous forces in the flow. For pipe flows, the Reynolds number can be computed as $\mathrm{Re} \equiv Ud/\nu$, where d is the diameter of the pipe and ν is the kinematic viscosity of the fluid. In rough-walled pipe flows, f depends on Re and the relative roughness, which is defined as the ratio r/d, where r is the average size of roughness elements that line the wall. (Here we will often refer to the relative roughness simply as "roughness.")

The classic set of experiments of the frictional drag in pipe flows was carried out by Nikuradse in 1933 [9]. Almost 80 years later, it remains the most comprehensive single set of experiments on turbulent pipe flows, notwithstanding the significant technical advancement over the decades [15].

Nikuradse's data (Fig. 3.1) stretch over three orders of magnitude in Reynolds number and more than one order of magnitude in roughness. These data helped establish two important asymptotic regimes in turbulent pipe flows. We will refer to these regimes as the Blasius regime and the Strickler regime.

The Blasius regime obtains in smooth-walled pipes and in hydraulically smooth pipes, where the frictional drag depends only on Re. Numerous mathematical expressions have been proposed to describe the relation between f and Re in this regime; for moderate turbulent strength (starting from $\mathrm{Re} \approx 2,500$ and up to $\mathrm{Re} \approx 100,000$), the experimental data on the Blasius regime (including the latest data from the Princeton superpipe) appear to be best represented [19] by the Blasius empirical scaling, $f \propto \mathrm{Re}^{-1/4}$ [59, 60].

The Strickler regime obtains in rough-walled pipes in the limit of large Re, where the frictional drag depends only on the roughness. Once again, numerous mathematical expressions have been proposed to describe the relation between f and r/d in this regime; a reasonable representation of the experimental data is given by the Strickler empirical scaling, $f \propto (r/d)^{1/3}$ [61].

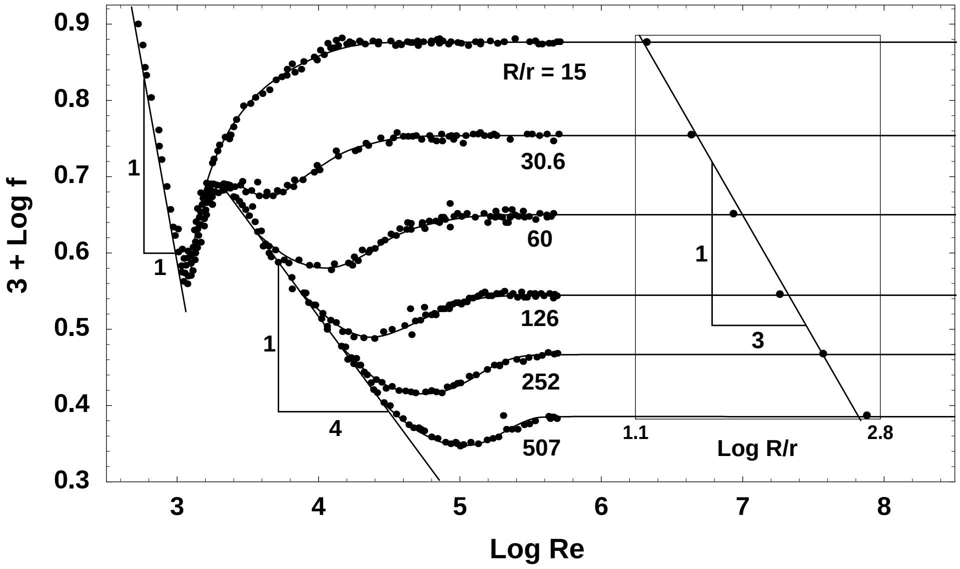

Figure 3.1: Nikuradse's data (taken from [1]). The data are shown as a log-log plot of f vs Re; the six curves correspond to six values of roughness. The Blasius empirical scaling, $f \sim \mathrm{Re}^{-1/4}$, and the Strickler empirical scaling, $f \sim (r/d)^{1/3}$, are marked.

Many attempts have been made to account theoretically for Nikuradse's data. The earliest theory came shortly after the experiments of Nikuradse: it was the soon-to-become-classic theory of Ludwig Prandtl [5]. Numerous variants [5, 19, 15] and alternatives [20, 21] of Prandtl's theory have since been proposed. Nevertheless, as all these theories have been predicated on dimensional analysis and similarity assumptions, without reference to the spectral structure of the turbulent fluctuations, they cannot be used to reveal what we call the "spectral link", that is to say, the missing link between the frictional drag and the turbulent spectrum.

3.2 The spectral link

Consider the flow of a fluid through a pipe of diameter d. The mean velocity of the flow is U. The wall of the pipe is lined with roughness elements of size r. The roughness elements are coated by a viscous layer of thickness $a\eta$, where a is a dimensionless constant and η is the viscous length scale of Kolmogorov's phenomenological theory of turbulence. (Note that η is set by the turbulent spectrum.) We call W an imaginary wetted surface that is tangent to the peaks of the viscous layer; W separates two different regions in the flow (Fig. 3.2): the outer stream and the coves (i.e., the spaces between successive roughness elements). We argue that due to the dissipative effects of the viscous layer and the sheltering effects of the roughness elements, the momentum of the flow in the cove is negligible. By contrast, the momentum of the flow in the outer stream scales as ρU. Therefore, there exists a momentum contrast across W, and this momentum contrast is proportional to $\rho U - 0 = \rho U$.

We seek to obtain an expression for the shear stress τ between the rough wall and the flow. The shear stress is effected by turbulent eddies that straddle W and transfer momentum across W. Consider an eddy of size σ that straddles W (Fig. 3.2). This eddy transfers fluid of high horizontal momentum downwards across W and fluid of negligible horizontal momentum upwards across W. The net rate of transfer of momentum across W scales with the velocity normal to W, i.e., the revolving velocity of the eddy, u_σ. The shear stress effected by the eddy of size σ is proportional to the product of the rate of momentum

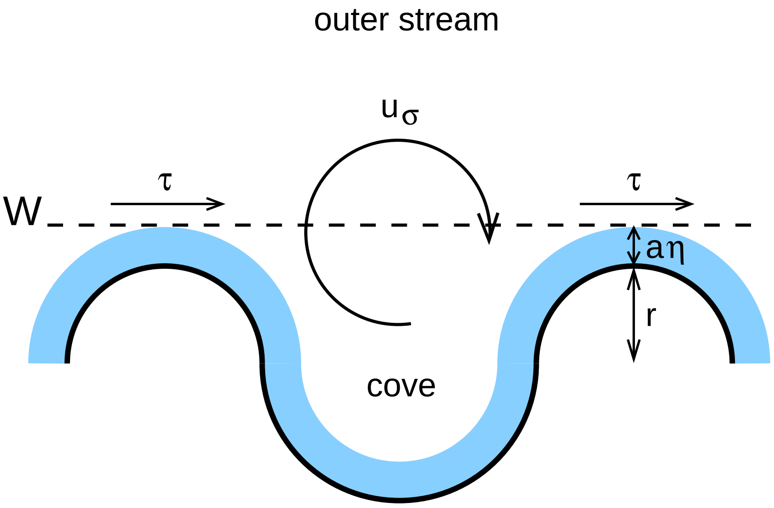

Figure 3.2: Schematic of roughness elements of size r covered by a viscous layer of thickness $a\eta$. The distance between roughness elements is roughly equal to r. The dashed line represents the imaginary wetted surface W that is tangent to the peaks of the viscous layer. The region above W is the outer stream with high momentum. The region below W is the cove with negligible momentum. After [1].

transfer (which scales as u_σ) and the momentum contrast (which scales as ρU). Thus, we can write $\tau \propto (\rho U)u_\sigma$ for the shear stress effected by the eddy of size σ.

A key assumption of the theory is that u_σ can be calculated from the turbulent spectrum $E(k)$ as

$$u_\sigma = \left(\int_{1/\sigma}^{\infty} E(k)dk \right)^{1/2}. \tag{3.1}$$

For future reference, note that since $E(k) > 0$, the larger the eddy, the higher the velocity of the eddy.

While eddies of many sizes contribute to the total momentum transfer across W, we seek to identify the *dominant eddy* that provides the dominant contribution to the shear stress. To that end, consider the following geometric argument. Let us denote the size of the cove by s, where $s = r + a\eta$ (see Fig. 3.2). An eddy of size much larger than s does not contribute a significant momentum transfer across W since its normal velocity component at W is small. Now consider eddies of size $\sigma \leq s$. The contribution to the momentum transfer across W by each of these eddies is proportional to the revolving velocity of the eddy. Since the larger the eddy, the higher its velocity, the contribution of the eddy of size s dominates the expression for shear stress. Therefore, we identify the eddy of size s to be the dominant eddy and conclude that the shear stress between the flow and the rough wall is given by $\tau \propto \rho U u_s$. Hence the frictional drag is:

$$f = \frac{\tau}{\rho U^2} \propto \frac{\rho U u_s}{\rho U^2} \propto \frac{u_s}{U}, \qquad \text{where } s = r + a\eta. \tag{3.2}$$

The close tie between the frictional drag and the turbulent spectrum is apparent in (3.2). Both u_s and η are spectral quantities. To make the relation explicit for u_s, we substitute (3.1) in (3.2) and find

$$f \propto \frac{1}{U}\left(\int_{1/r+a\eta}^{\infty} E(k)dk\right)^{1/2}. \tag{3.3}$$

Thus, the frictional drag is but a transform of the turbulent spectrum. Equation (3.3) is the mathematical statement of the spectral link.

3.3 Predictions of the spectral theory for three-dimensional turbulence

To arrive at an expression for the turbulent spectrum, $E(k)$, in 3D turbulence consider the energy cascade argument by Kolmogorov [7]. Building on Richardson's concept of a cascade of eddies [62], Kolmogorov argued that for a range of eddy sizes, as the larger eddies split into smaller eddies in a cascade, the turbulent energy per unit mass and per unit time, ε, is transferred without any viscous losses at each step of this cascade. This range is known as the inertial range and the process is known as the energy cascade. Kolmogorov argued that in the inertial range $E(k)$ (with dimension $[L]^3/[T]^2$) is solely a function of ε (with dimension $[L]^2/[T]^3$) and the wavenumber k (with dimension $1/[L]$). Thus, from dimensional analysis

$$E(k) \propto \varepsilon^{2/3} k^{-5/3}. \tag{3.4}$$

The above equation, which provides an expression for $E(k)$ in 3D turbulence, is referred to as the 5/3 law of Kolmorogov.

To obtain an expression for ε consider the following argument. For an eddy of size σ, the turbulent energy per unit mass is u_σ^2 and the time scale associated with the splitting of the eddy, from dimensional analysis, scales as σ/u_σ. Thus, for the turbulent energy per unit mass and per unit time, ε, we get

$$\varepsilon \propto \frac{u_\sigma^2}{\sigma/u_\sigma} \propto \frac{u_\sigma^3}{\sigma}. \tag{3.5}$$

Since equation (3.5) is true for eddies of all sizes in the inertial range, it applies to the largest eddy in the flow, whose characteristic length and velocity is proportional to d and U, respectively. Thus we get the following relation:

$$\varepsilon \propto \frac{U^3}{d}. \tag{3.6}$$

To find the relation between the characteristic length and velocity of the dominant eddy, we substitute the expressions of the energy spectrum (3.4) and the energy rate (3.6) in equation (3.1) and obtain

$$u_s \propto U \left(\frac{s}{d}\right)^{1/3}, \qquad \text{where } s = r + a\eta. \tag{3.7}$$

(The above expression can also be obtained by eliminating ε between equations (3.5) and (3.6).) The frictional drag (3.2) thus becomes:

$$f \propto \left(\frac{s}{d}\right)^{1/3} = \left(\frac{r + a\eta}{d}\right)^{1/3}. \tag{3.8}$$

Now we need to find how η depends on Re so as to use the above expression to find how f depends on Re and roughness.

To find an expression for the viscous length scale η we define a local Reynolds number, with the velocity and length scales as u_η and η, respectively, as $u_\eta \eta/\nu$. Since Reynolds number is a relative measure of the contributions between inertial and viscous effects and since for an eddy of size η these effects are equally important, we define $u_\eta \eta/\nu \equiv 1$. By applying equation (3.7) to an eddy of size η we obtain

$$\eta \propto d\mathrm{Re}^{-3/4}. \tag{3.9}$$

By substituting the above expression of η into equation (3.8), we have the final formula for f in 3D turbulent flows [1]:

$$f \propto \left(\frac{r}{d} + a\mathrm{Re}^{-3/4}\right)^{1/3}. \tag{3.10}$$

We are now ready to understand the spectral underpinnings of the two asymptotic regimes in Nikuradse's data. In the limit $r/d \to 0$, the momentum transfer is dominated by eddies of size $s \propto \eta$, and equation (3.10) yields $f \propto \mathrm{Re}^{-1/4}$. Thus, the theory predicts the Blasius scaling in the Blasius regime. In the limit $\mathrm{Re} \to \infty$, the momentum transfer is dominated by eddies of size $s \propto r$, and equation (3.10) yields $f \propto (r/d)^{1/3}$. Thus, the theory predicts the Strickler scaling in the Strickler regime.

The spectral theory of the frictional drag consists of two ingredients: the momentum-transfer model and the turbulent spectrum. The former allows us to ascertain the dependence of the frictional drag on the velocity of the dominant eddy, which velocity is responsible for transferring momentum and create the shear stress. The later gives an explicit relation between the velocity of the dominant eddy and the size of that eddy.

In 3D turbulent flows, there is only one type of turbulent spectrum, that given by equation (3.4). Nevertheless, the spectral link is not restricted to this form of turbulent spectrum. In 2D turbulent flows (a kind of flow that can be realized in a soap film), other spectra are possible, and for each type of spectrum the momentum-transfer model can be used to predict the corresponding generalized Blasius scaling and generalized Strickler scaling.

3.4 Spectra in two-dimensional turbulence

We start by reviewing some aspects of 2D turbulence that set 2D turbulence apart from its 3D counterpart. The classic works by Kraichnan and Batchelor [37, 38] first elucidated the unique features of 2D turbulence. In 3D turbulence, vortex stretching provides a principal mechanism for transfer of energy from larger eddies to smaller eddies. By contrast, one of the most distinctive features of 2D turbulence is the absence of vortex stretching. This can be easily seen by examining the equation for the vorticity, $\boldsymbol{\omega}$ [63]:

$$\frac{D\boldsymbol{\omega}}{Dt} = \boldsymbol{\omega} \cdot \nabla \mathbf{u} + \nu \nabla^2 \boldsymbol{\omega} \tag{3.11}$$

In a two-dimensional flow, only one component of the vorticity is non-zero and we assume that it is in the z direction ($\boldsymbol{\omega} = (0, 0, \omega_z)$). Then the velocity lies in the (x, y) plane. This implies that the “vortex-stretching” term, $\boldsymbol{\omega} \cdot \nabla \mathbf{u}$, vanishes throughout the flow. Further, if we take the dot product of (3.11) and $\boldsymbol{\omega}$ and average it spatially, we obtain the evolution equation for the enstrophy $\Omega \equiv \langle \boldsymbol{\omega}^2 \rangle /2$:

$$\frac{D\Omega}{Dt} = -\nu \left\langle (\nabla \omega)^2 \right\rangle . \tag{3.12}$$

The above equation shows that in 2D turbulence, enstrophy of a material point is dissipated only via viscous effects. In the inertial range, by definition, dissipation due to viscosity is negligible and hence the enstrophy is conserved. However, at small scales, the right-hand term in equation (3.12) becomes significant because of large vorticity gradients. An enstrophy sink at small length scales suggests that enstrophy is transferred from larger length scales and dissipated at length scales comparable to the viscous length scale. A stationary state may be reached if the enstrophy dissipation rate $\beta \equiv \nu \left\langle (\nabla \omega)^2 \right\rangle$ is equal to the enstrophy injection rate and is independent of the fluid viscosity.

In addition to conserving the enstrophy rate, 2D turbulent flows, similar to 3D turbulent flows, can also conserve energy rate. The fact that there are two conserved transport quantities, energy rate and enstrophy rate, in the inertial range of 2D turbulence poses a dilemma: two distinct cascades are possible. To explain this situation, Kraichnan theoretically argued [37] that there exists a dual cascade, wherein the enstrophy may cascade from larger to smaller scales (the direct enstrophy cascade), while the energy may cascade in the opposite direction (the inverse energy cascade). To obtain an expression for the energy spectrum, $E(k)$, corresponding to these cascades, we again invoke dimensional analysis with the set of relevant parameters in the inertial range being either β and k (for enstrophy cascade), or ε and k (for inverse energy cascade). The energy spectrum in the enstrophy cascade can be written as:

$$E_\beta(k) \propto \beta^{2/3} k^{-3}, \tag{3.13}$$

whereas in the inverse energy cascade, the expression for the energy spectrum remains the same as in 3D turbulence:

$$E_\varepsilon(k) \propto \varepsilon^{2/3} k^{-5/3}. \tag{3.14}$$

Consider the following physical picture of Kraichnan's argument of a dual cascade. Suppose that we disturb the flow by injecting energy at a wavenumber k_i. For $k < k_i$, the dominant transport quantity is energy rate and $E(k)$ is determined by equation (3.14). For $k > k_i$, the dominant transport quantity is enstrophy rate and $E(k)$ is determined by equation (3.13). The injection wavenumber k_i marks the transition point between the two cascades.

In most reported experiments, the dominant cascade has been the enstrophy cascade, with little or no hints of an inverse energy cascade. In our experiments, we not only obtain flows with pure enstrophy cascade, but also, for the first time, we obtain flows with pure inverse energy cascade. This has been a crucial achievement in our research, because in order to test the spectral link it is important to be able to realize flows with a definite type of spectrum.

3.5 Predictions of the spectral theory for two-dimensional turbulence

By denoting the spectral exponent of the turbulent spectrum as α, we can encompass both the enstrophy cascade, for which $\alpha = 3$, and the inverse energy cascade, for which $\alpha = 5/3$. A generalized expression for the turbulent spectrum can be written as:

$$E(k) \propto U^2 d^{1-\alpha} k^{-\alpha}. \tag{3.15}$$

By substituting the generalized energy spectrum into equation (3.1) and evaluating it at the size of the dominant eddy, we obtain the eddy's characteristic velocity:

$$u_s \propto U \left(\frac{s}{d}\right)^{(\alpha-1)/2}, \qquad \text{where } s = r + a\eta. \tag{3.16}$$

The viscous length scale η also varies with the spectral exponent. By following the steps outlined earlier (see the discussion before equation (3.9)), we get:

$$\eta \propto d\mathrm{Re}^{-2/(\alpha+1)}. \tag{3.17}$$

The frictional drag (3.2) then follows as:

$$f \propto \left(\frac{r}{d} + a\mathrm{Re}^{-2/(\alpha+1)}\right)^{(\alpha-1)/2}. \tag{3.18}$$

In the limit of zero roughness, $r/d = 0$, equation (3.18) becomes [27]

$$f \propto \mathrm{Re}^{(1-\alpha)/(1+\alpha)}, \tag{3.19}$$

which is a generalized form of the Blasius scaling. For 2D turbulent flows in inverse energy cascade, $\alpha = 5/3$, and (3.19) yields $f \propto \mathrm{Re}^{-1/4}$, i.e. the same scaling as in 3D turbulent flows. For 2D turbulent flows in enstrophy cascade, $\alpha = 3$, and (3.19) yields $f \propto \mathrm{Re}^{-1/2}$.

In the limite $\mathrm{Re} \to \infty$ and fixed roughness, equation (3.18) becomes

$$f \propto \left(\frac{r}{d}\right)^{(\alpha-1)/2}, \tag{3.20}$$

which is a generalized form of the Strickler scaling. For 2D turbulent flows in inverse energy cascade, $\alpha = 5/3$, and (3.19) yields $f \propto (r/d)^{1/3}$, i.e. the same scaling as in 3D turbulent flows. For 2D turbulent flows in enstrophy cascade, $\alpha = 3$, and (3.19) yields $f \propto (r/d)$.

In the next chapter, we test experimentally the predictions of equation (3.19). To that end, we perform extensive experiments on turbulent 2D soap-film flows.

Chapter 4

Test of the spectral theory in smooth-walled soap-film flows

The experiments described in this chapter* are aimed at testing the predictions of the spectral theory of the frictional drag in smooth–walled 2D turbulent flows with enstrophy cascade (spectral exponent $\alpha = 3$) and inverse energy cascade (spectral exponent $\alpha = 5/3$. Specifically, these predictions are as follows (see Chapter 3 for details).

- For the inverse energy cascade,

  $$f \propto \mathrm{Re}^{-1/4}, \tag{4.1}$$

  where the Reynolds number Re is computed with the width of the soap-film flow, to be denoted w. This scaling coincides with the Blassius empirically scaling, which is known to obtain in 3D turbulent flows with the energy cascade (whose spectral exponent is the same as for the inverse energy cascade).

- For the enstrophy cascade,

  $$f \propto \mathrm{Re}^{-1/2}. \tag{4.2}$$

  This scaling is unprecedented.

The 2D turbulent flows are realized in soap films. To our knowledge, these are the first-ever experimental measurements of the frictional drag in soap-film flows.

---

*Part of the work described in this chapter has been published in [41]

4.1 Experimental setups

In one of our experimental setups, a soap film hangs between two long, vertical, mutually parallel wires a few centimeters apart (Fig. 4.1a). We also use a slightly modified setup (Fig. 4.2a). In this modified setup, we replace the parallel portions of the wires by two blades, one rough and one smooth. (A detailed description of the setups is provided in section 5.2).

Driven by gravity, a steady vertical flow soon becomes established within the film. Then, the thickness h of the film is roughly uniform on any cross section of the film, typically $h \approx 10\,\mu\text{m}$, much smaller than the width w and the length of the film (Fig. 4.1a, Fig. 4.2a). As a result, the velocity of the flow lies on the plane of the film, and the flow is 2D.

We make the flow turbulent with the enstrophy cascade by piercing the film with a comb, as indicated in Fig. 4.1a, so that the flow is stirred as it moves past the teeth of the comb. (The comb is the 2D counterpart of the grid used to generate turbulence in 3D flows.) To generate turbulent flows with inverse energy cascade, we use the modified setup of Fig. 4.2a, with no comb present. Vortices shedding from the rough wall are continuously transported to the smooth side of the channel, ensuring a constant flux of energy.

To visualize the flow, we cast monochromatic light on a face of a film and observe the interference fringes that form there. These fringes (Fig. 4.1b, 4.2b) reflect small changes in the local thickness of the film. (The thickness is constant along a fringe; it differs by a fraction of the wavelength of the light, or a fraction of a μm, between any two successive fringes.) The small changes in thickness in turn reflect small changes in the absolute value of the instantaneous velocity of the flow [36]. Thus the photographs of Figs. 4.1b and 4.2b may be interpreted as maps of the instantaneous spatial distribution of turbulent fluctuations.

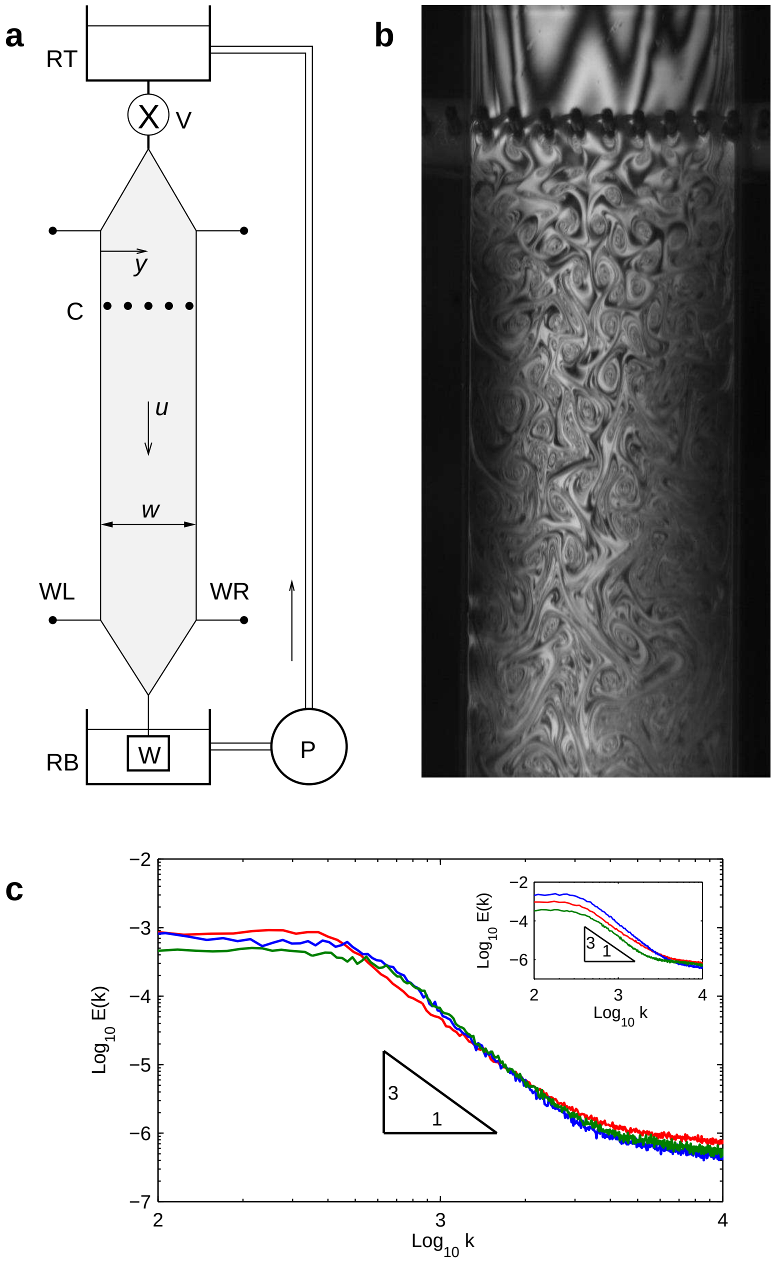

Figure 4.1: Experimental setup used to study steady, gravity-driven, 2D soap-film flows in *enstrophy cascade*. **(a)** Wires WL and WR are thin nylon wires (diameter = 0.5 mm) kept taut by weight W. The film hangs from the wires; its width increases from 0 to w over an expansion section, then remains constant and equal to w over a section of length ≈ 1 m. Reservoir RT contains a soapy solution (2 % Dawn Nonultra in water; $\nu = 0.01\,\mathrm{cm}^2/\mathrm{s}$), which flows through valve V and into the film. After flowing through the film, the soapy solution drains into reservoir RB and returns to reservoir RT via pump P. Turbulence is generated by comb C of tooth diameter ≈ 0.5 mm and tooth spacing ≈ 3 mm. We perform all measurements at a distance of at least 10 cm downstream of the comb. Axis y ($0 \le y \le w$) has its origin at wire WL, as indicated. **(b)** Interference fringes in yellow light (wavelength = 0.6 μm) make it possible to visualize the generation of 2D turbulence from the comb. **(c)** Typical log-log plots of the spectrum $E(k)$, from LDV measurements performed on points of the film close to one of the wires and (inset) along the centerline of the flow

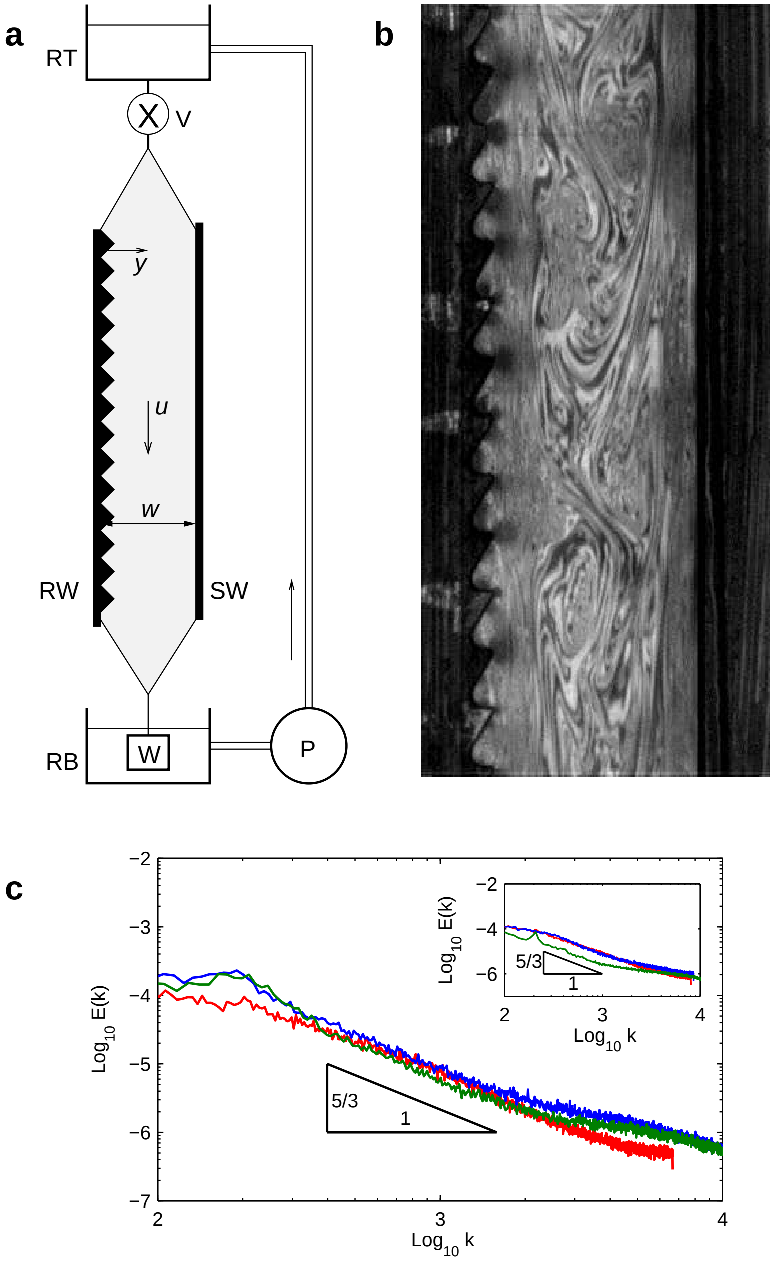

Figure 4.2: Experimental setup used to study steady, gravity-driven, 2D soap-film flows in *inverse energy cascade*. **(a)** Two blades RW and SW replace the parallel portions of two wires in the setup shown in Fig. 4.1. The blades are 1.2 m long and 0.5 mm thick. The distance between the blades is the film width w. Turbulence is generated by the rough blade RW of tooth size and spacing $\approx 2\,\mathrm{mm}$. All measurements were made at a distance of at least 70 cm from the top of the blades. The friction factor was measured on the smooth side SW of the channel. **(b)** Interferometric graph of the film shows generation of 2D turbulence from the rough blade. **(c)** Typical log-log plots of the spectrum $E(k)$, from LDV measurements performed on points of the film close to the smooth side SW and (inset) along the centerline of the flow

4.2 Spectra

We compute the spectrum $E(k)$ at numerous points on a film from measurements performed with a Laser Doppler Velocimeter (LDV). We start by measuring the vertical component $u(t)$ of the instantaneous velocity at a point on the film using a LDV with a sampling rate of 5 kHz. By performing measurements over a time period of about $10\,\mathrm{s}$, we collect a time series $u(t_i)$. From the time series we compute the local mean velocity u as the time average of $u(t_i)$, $u = \langle u(t_i) \rangle$. From the same time series $u(t_i)$ we compute the local turbulent spectrum (more precisely, the longitudinal turbulent spectrum). To that end, we invoke Taylor's frozen-turbulence hypothesis [64] to perform a space-for-time substitution $t \to x/u$ on the time series $(u(t_i) - u)$ to obtain a space series $v(x_i) = (u(x_i/u) - u)$, where $x_i = ut_i$. (The frozen-turbulence hypothesis is justified because in all our experiments the root mean square of the velocity fluctuations is less than 20% of u[65].) The spectrum $E(k)$ is the square of the magnitude of the coefficients of the discrete Fourier transform of $v(x_i)$.

In Fig. 4.1c we show a few typical log-log plots of E vs. k for comb-generated turbulence. The slope of these plots represents the spectral exponent α; in our experiments the slope is slightly larger than 3, consistent with prior experiments with soap-film flows [66, 36] and close to the theoretical value of α for the enstrophy cascade ($\alpha = 3$).

In Fig. 4.2c we show a few typical log-log plots of E vs. k for roughness-generated turbulence. The slope of these plots is slightly smaller that 5/3, close to the theoretical value of α for the inverse energy cascade ($\alpha = 5/3$). To our knowledge, no one has previously realized turbulence with a pure inverse energy cascade in a soap film.

4.3 Frictional drag

In what follows we describe a procedure to obtain the mean velocity and the frictional drag. Although this procedure applies for turbulent flows in both experimental setups, we illustrate for the conventional setup (comb-generated turbulence, enstrophy cascade). Note that in the modified setup (roughness-generated turbulence, inverse energy cascade) the frictional drag is measured on the smooth side of the channel.

By using Laser Doppler Velocimeter we can measure the mean (time-averaged) velocity u at any point on the film. Successive measurements of u along a cross section of the film gives the "mean velocity profile" $u(y)$ of that cross section. In Fig. 4.3a we show a few typical plots of $u(y)$ over the entire width of the film (i.e., from wire to wire, or for $0 \leq y \leq w$). From a mean velocity profile we compute the mean velocity of the flow as $U = (1/w)\int_0^w u(y)dy$, and the Reynolds number of the flow as $\mathrm{Re} = Uw/\nu$.

In Fig. 4.3b we show a few typical plots of $u(y)$ close to one of the wires, where u depends linearly on y on a narrow (about 0.2 mm) viscous layer. (We have verified that the Reynolds shear stress $\tau_{\mathrm{Re}} = \rho \left\langle (u(t_i) - u)(v(t_i) - v) \right\rangle$ vanishes in the viscous layer; Figs. 4.3c and d.) From the slope G of a mean velocity profile in the viscous layer, we compute the shear stress between the flow and the wire as $\tau = \rho\nu G$, and the frictional drag as $f = \tau/\rho U^2 = \nu G/U^2$.

An apparent slip velocity, U_S, is conspicuous in the plots of Fig. 4.3b, and is likely to represent 3D and surface-tension effects associated with the complex flow at the contact between a film and a wire. The value of U_S tends to lessen where we use thinner wires or brand new wires. By using a variety of wires, we have been able to realize several flows with the same value of Re but widely differing values of U_S. We have verified that the frictional drag of these flows is the same within experimental error (e.g., Fig. 4.4), in spite of the widely differing values of U_S. We conclude that the frictional drag does not depend on the apparent slip velocity (except through the Reynolds number).

Using the two separated setups and the procedure described above, we obtain values of f and the attendant values of Re for turbulent flows with both types of spectra. In Fig. 4.5a we show a log-log plot of f vs. Re for turbulent flows with the enstrophy cascade. The plot consists of five sets of data points from numerous turbulent soap-film flows. The first four sets were taken by the author at Pittsburgh, and the last set was taken at Université Bordeaux by Hamid Kellay in an independent experimental setup. The cloud of data points

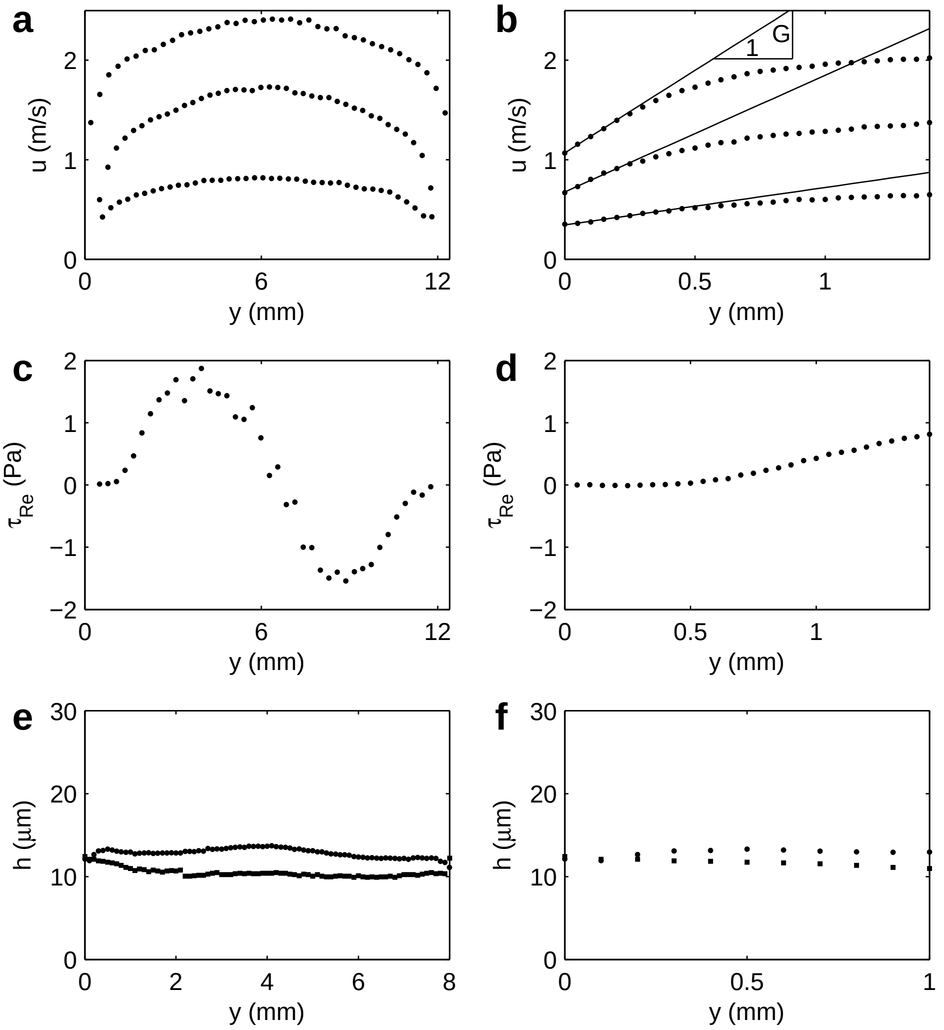

Figure 4.3: The mean velocity profile $u(y)$, the Reynolds shear stress profile $\tau_{\text{Re}}(y)$, and the thickness profile $h(y)$ in turbulent soap-film flows. **(a)** Typical plots of $u(y)$ in a film of width $w = 12\,\text{mm}$, for $\text{Re} = 7890, 17600$ and 25900. From LDV measurements. **(b)** The same as in **a** but close to one of the wire. In the viscous layer the slope of $u(y)$ is constant, $du(y)/dy = G$. Points on the film closer than $\approx 20\mu\text{m}$ (the diameter of the beam of the LDV) from the edge of the wire cannot be probed with the LDV; thus the first data point, which we position at $y = 0$, is at a distance of $\approx 20\mu\text{m}$ from the edge of the wire. **(c)** Plot of $\tau_{\text{Re}}(y)$ in a film of width $w = 12\,\text{mm}$, for $\text{Re} = 17600$. **(d)** The same as in (c) but close to one of the wires. The Reynolds shear stress vanishes in the viscous layer (compare with the plot in **b**). **(e)** Typical plots of $h(y)$ in a film of width $w = 8\,\text{mm}$, for $\text{Re} = 9430$ and 13000. From fluorescent-dye measurements (see Appendix 5.4.2). **(f)** The same as in **e** but close to one of the wires. The thickness of the film is nearly uniform in the viscous layer (compare with the plots in **b**).

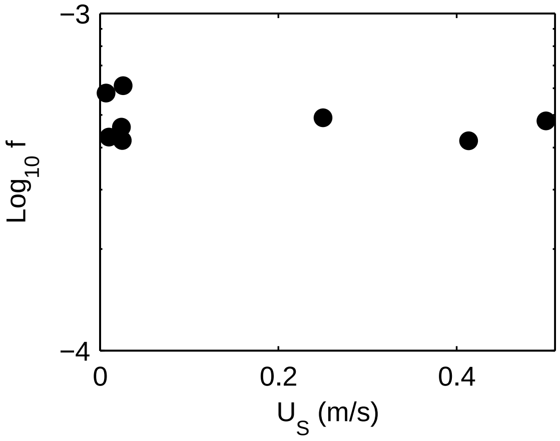

Figure 4.4: Log-linear plot of the frictional drag f vs. the apparent slip velocity U_S in 2D turbulent soap-film flows of Reynolds number $\text{Re} = 20000$.

is consistent with the scaling, $f \propto \text{Re}^{-1/2}$, in accord with the prediction of the spectral theory of the frictional drag (equation (4.2)).

In Fig. 4.5b we show a log-log plot of f vs. Re for turbulent flows with the inverse energy cascade. The plot consists of several sets of data points from numerous turbulent soap-film flows. All the sets were taken by the author at Pittsburgh. The cloud of data points is consistent with the scaling, $f \propto \text{Re}^{-1/4}$, in accord with the prediction of the spectral theory of the frictional drag (equation (4.1)).

4.4 Discussion

From our experiments with two-dimensional soap-film flows we infer that the long-standing and widely-accepted theory [5] of the frictional drag between a turbulent flow and a wall is incomplete. This classical theory does not take into account the structure of the turbulent fluctuations, and cannot distinguish between two-dimensional and three-dimensional turbulent flows. Our data on soap-film flows, as well as the available data on pipe flows, are, however, consistent with the predictions of the spectral theory of frictional drag (Chapter 3). This new theory perforce relates the frictional drag to the turbulent spectrum, and is

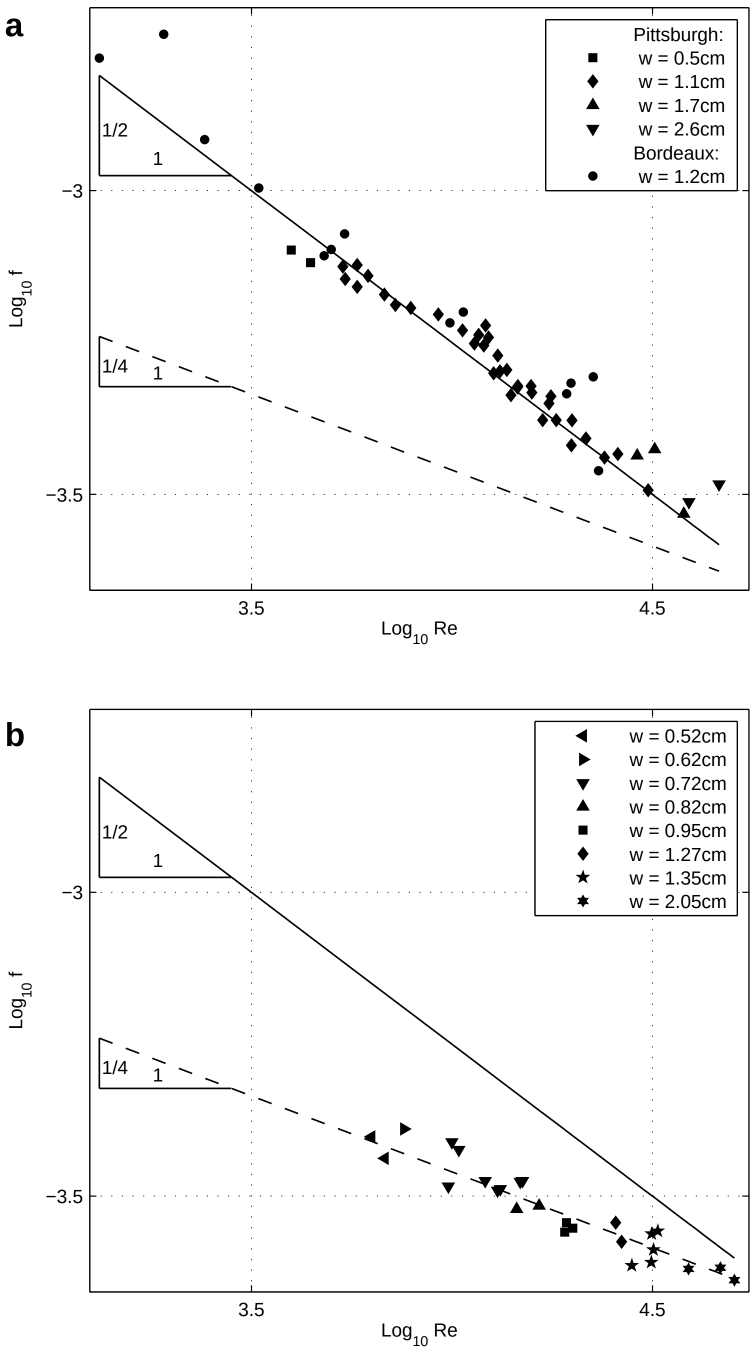

Figure 4.5: **(a)** Frictional drag measurements of 2D turbulent soap-film flows with the *enstrophy cascade*: log-log plot of f vs. the Reynolds number Re for $1300 \leq \mathrm{Re} \leq 46000$, from independent experiments performed in Pittsburgh and Bordeaux. The cloud of data points may be represented as a straight line of slope 1/2, consistent with the scaling $f \propto \mathrm{Re}^{-1/2}$. **(b)** Friction drag measurements of 2D turbulent soap-film flows with the *inverse energy cascade*: log-log plot of f vs. Re for $6300 \leq \mathrm{Re} \leq 50600$. The cloud of data points may be represented as a straight (dashed) line of slope 1/4, consistent with the scaling $f \propto \mathrm{Re}^{-1/4}$.

sensitive to the dimensionality of the flow via the dependence of the turbulent spectrum on the dimensionality. Our findings lead us to conclude that the macroscopic properties of both three-dimensional and two-dimensional turbulent flows are closely linked to the turbulent fluctuations. In addition, our findings serve to underscore the value of using two-dimensional soap-film flows to test and extend our understanding of turbulence.

Chapter 5

Apparatus and experimental techniques

Soap films have long attracted the attention of researchers not only because of their fascinating beauty but also because of their applications in science and technology [67, 68]. In the laboratory, soap-film flows are perhaps the best possible proxy of two-dimensional flows and have been widely used in experimental work on 2D turbulence [36].

Experimental setups used to produce soap-film flows have been developed and constantly improved in the last 15 years, starting with pioneers such as Couder and Garib [69, 2, 42, 43]. Among many designs, the gravity-driven soap-film channel developed by Kellay and Goldburg [66, 50] has been most widely used. An important advantage of this type of channel for the research discussed in this dissertation has been its the ability to sustain flows in a wide range of velocities.

In this chapter we present a detailed description of a gravity-driven soap-film channel and some improvements we have made to its design. We also discuss the experimental techniques we have used to measure properties of soap-film flows, with an emphasis on the refinements that have been important to our study.

5.1 Conventional soap-film channels

5.1.1 Overview

In Fig. 2.1, a typical setup of a soap film channel is shown. A soapy solution is contained in the upper reservoir and flows down in a pipe to an injection point through valve V. The valve is used to adjust the flow speed by varying the volumetric rate Q.

From the injection point the soapy solution forms a soap film between two nylon wires. A weight W is tied to the lower ends of the two supporting wires to keep the wires taunt. The soap film is driven by gravity, and a soap-film flow is established in the film. Typically, the soapy solution travels through three sections: an expansion section where the film width increases, a measurement section where the film width is constant, and a contraction section where the wires are brought together. The film width w is defined as the distance between the two wires in the measuring section.

After drifting off from the wires to a lower reservoir, the soapy solution is circulated back to the upper reservoir by a pump P. An overflow pipe is installed in the upper reservoir to keep the solution level there constant. The fixed pressure head at the injection point produces steady-state soap-film flows.

The channel's components are held in place by aluminum rods attached to an optical table (not shown). The distance between the lower and upper reservoir can be as large as 2.5 m, providing a maximum length of about 2 m to the measurement section.

5.1.2 Fluid injection

The fluid injection scheme is responsible for feeding soapy solution to the soap-film channel at a constant rate. It includes a small nozzle connected with the upper reservoir through a valve and a silicone rubber pipe. In the current setup, we use a glass nozzle in which the conical tip has an elliptic cross section. If a glass nozzle is not available, one can use a plastic nozzle with the tip being squeezed to change the cross section from circular to elliptic.

We observe that the uniformity of the film thickness depends sensitively on the cross sectional shape of the tip; an elliptic shape seems to produce the most satisfactory results. Typically, the tip's cross section is about 2 mm by 0.5 mm in size. Larger tips are preferable for high velocity flows, but smaller tips give a more uniform film thickness. The uniformity of film thickness in the measurement section is also affected by how the film width increases in the expansion section. A more gradual expansion generally produces a more uniform film thickness.

In our soap film channel, the expansion section stretches between 20 cm and 100 cm while the film width is expanded from 1 mm to 5,cm. The flow exiting the expansion section has a velocity that ranges from 0.5 m/s to 2 m/s. For this reason, the expansion length is an additional parameter to control flow velocity in the measurement section.

5.1.3 Film termination

A flowing soap film can be terminated in many ways, normally by tying two wires together (Fig. 5.1a). The film in the contraction section has a small velocity and can become so thick that it is possible to poke the film with a dry rod without breaking the film. The disturbances associated with the contraction section can propagate up into the measurement section.

The length of the contraction section can be varied between 10 cm and 50 cm. Although a longer contraction section helps to produce more stable films, in the course of the present research we discovered that the contraction section can be completely omitted if the flow rate is moderate. In that case, the fluid plunges directly into the lower reservoir (Fig. 5.1b). By omitting the contraction section, we have been able to eliminate disturbance in the lower part of the measurement section. This has been particularly useful in the study of the abrupt jump in the film thickness discussed in chapter 2.

5.1.4 Supporting wires

The supporting wires WL and WR (Fig. 2.1) are usually nylon fishing lines roughly 0.5 mm in diameter. Thinner lines cause film rupture more often. We keep wires WL and WR separate by tying lateral wires and pulling them apart. The pull wires should be very thin (~ 0.1 mm) to cause the least intrusion to the flow.

As noted earlier, wires WL and WR are kept taut by hanging a weight W at the lower

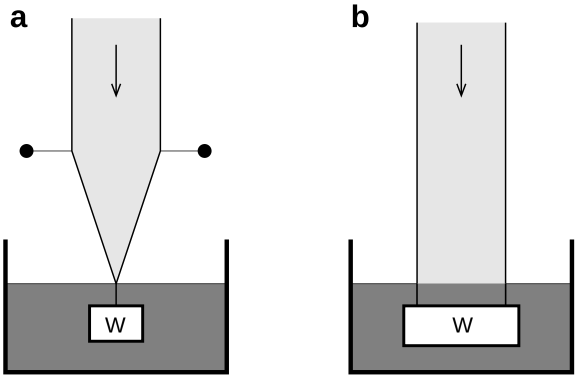

Figure 5.1: Different ways to terminate the film. **(a)** The film is terminated by contracting two wires together. **(b)** The film is terminated by letting the fluid plunge into the lower reservoir.

end (Fig. 5.1). It is practical to immerse the weight in the lower reservoir, and it has the advantage of damping any lateral oscillations of the weight. The weight should be heavy enough to prevent the wires from bowing inward due to the film's surface tension. To minimize reduction in the film width one can either tie more lateral wires or use the improved channel described in section 5.2.

5.1.5 Soapy solution

By adding soap into water, soap surfactants reduce the surface tension of the water and help prevent rupture of the film. There are many choices of soap, including sodium dodecyl sulfate (SDS) and cetyltrimethyl-ammoninum bromide (CTAB) [53]. Hand soap also works. We used a soapy solution consisting of Down Nonultra detergent and distilled water, with optimal detergent concentration ranging from 1 % to 3 %. The viscosity of this solution is the same as the viscosity of water. Soap films resulting from the solution can last for hours. The solution is made fresh every one or two weeks, as it loses surfactants with usage and causes film rupture more easily.

5.1.6 Surrounding conditions

During the course of our study, we have found that soap films are very sensitive to disturbances from surrounding air. Any small air current causes fluctuations of the flow velocity, as well as oscillation of the film in the direction perpendicular to its plane. Measurements made under these conditions are unreliable.

We have avoided these problems by putting the entire channel in a tent made of thick canvas. Alternatively, air disturbances can be prevented by replacing the tent by a glass chamber and partially evacuate the air inside [50]. Although the latter method is better, it is undeniably expensive and difficult to operate. For our purposes, we have found it sufficient to enclose the experimentation area with a tent.

5.2 Modified soap-film channels

In this section we introduce a modified version of the soap film channel. With the new channel, we have been able to avoid a number of problems in the original design. Moreover, the new channel offers new features and flexibilities that are useful for our study of friction factor in 2D turbulent flows (chapter 3).

The most important modification of the soap-film channel is the replacement within the measurement section of the two supporting wires by two metal blades of 0.5 mm in thickness. The edges of the blades serve as guiding lines for the soap film, as shown in Fig. 5.2.

The expansion section remains bounded by wires as before. The wires of the expansion section are glued to the upper ends of the blades. Since the thickness of the blades is only 0.5 mm, it takes great care to glue a fishing wire to an edge of the blades. We recommend securing the wire by a fine metal wire (~ 0.05 mm in diameter) before gluing it to the edge by water-resistant epoxy.

To terminate the film, the lower ends of the blades are either submersed into the solution or connected to a contraction section as in the original design. We use two aluminum bars

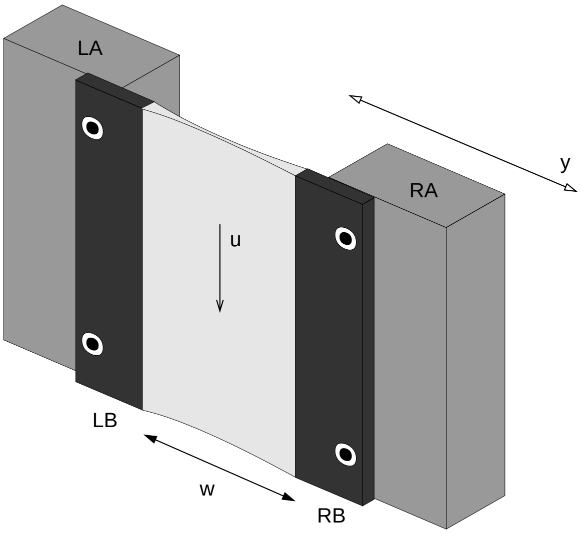

Figure 5.2: A portion of the modified soap-film channel. Two smooth blades LB and RB of thickness 0.5 mm support the film. The smooth edges can be made wavy, in which case the soap film flows in a 2D rough-walled channel (See Fig. 5.3). The blades are fastened to two aluminum bars LA and RA. The distance between the edges of the blade is w and can be varied from 0.5 cm to 5 cm by translating the aluminum bar RA in the y direction. Figure is not shown to exact scale.

as substrates to fasten the blades on. The distance between these bars, and therefore the film width w (Fig. 5.2), can be varied as one of them is attached to a linear translational stage. A proper alignment of the aluminum bars and the blades gives a constant film width regardless of vertical position.

At the lower ends of the channel, a soap film can become so thick that soap solution floods onto the blades. For this reason, it is essential to make the surfaces of the blades nonwettable by coating those surfaces with silicon-rubber sealant. The edges of the blades are left uncoated. The silicon-rubber sealant is also useful in protecting the blades from corrosion.

This step is crucial for a modified soap film channel, since the thickening of the film at its lower end is a distinct feature of this system. While the film is usually thought to be thinner and thinner as it falls down, the thickening of soap film at the lower end is counter-intuitive and deserve further investigation. We devote chapter 2 to explain the physical mechanism behind this thickening.

The modified soap-film channel, with its solid boundary, has allowed us to avoid a number of problems of channels supported by fishing wires. The modified channel is much stiffer than a wire channel, so there are no oscillations and no bowing of the channel's boundaries in the measurement section. The film width does not change with every change in the flow.

Furthermore, with the new channel it is possible to test 2D flows over rough walls. To this end, the smooth blades can be replaced by saw blades as shown in Fig. 5.3. This improvement is critical for our study of frictional drag that 2D turbulent flows exerts on rough walls. The turbulence generated by rough walls in our experiments also has distinct features from those of decaying turbulence. In the next section, we discuss different types of 2D turbulence and how to generate them in 2D flows.

5.3 Turbulence generation in two-dimensional soap-film flows

As the focus of this study is 2D turbulence in soap-film flows, in this section we review different types of turbulence that can be created experimentally in such flows. It would be incomplete not to mention stratified shallow layers of fluid as an alternative way to study 2D turbulence [34, 70, 71, 72]. However, in the scope of this dissertation, we limit ourself to discussing only 2D turbulence in soap-film channels.

In 2D turbulence there exists a double cascade process whereby energy may cascade from smaller to larger scales, while enstrophy (defined as the square of vorticity) may cascade in the opposite direction. The double cascade process, in principle, can be observed by calculating quantities such as the power energy spectrum of turbulent velocity fluctuations $E(k)$, where k denotes the wavenumber. If turbulence is generated at a length scale l_j, or correspondingly a wavenumber $k_j = 2\pi/l_j$, $E(k)$ is a power law of different exponent in two distinct regions. For $k < k_j$, $E(k) \propto k^{-5/3}$ (the inverse energy cascade), and for $k > k_j$, $E(k) \propto k^{-3}$ (the enstrophy cascade) [38, 37].

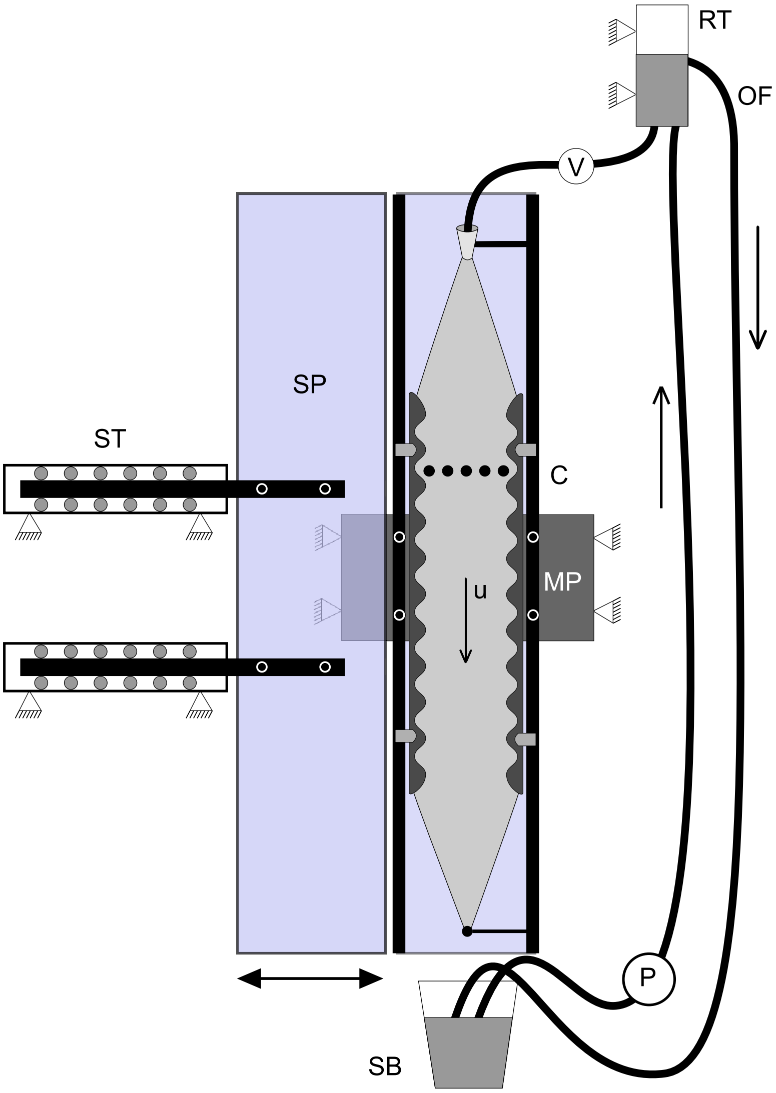

Figure 5.3: Experimental setup used to study steady, gravity-driven 2D soap-film flows in rough channels. Two rough blades (0.5 mm in thickness) are used to supported the film. The blades are fastened to two aluminum t-slotted frames held by a fixed metal plate MP. The upper end of each blade is connected to a nozzle made of glass by a fishing wire of 0.5mm in diameter. These wires guide the film from the nozzle to the blades. The blades's lower ends are glued to fishing wires to form a contraction section. Reservoir RT contains a soapy solution, which flows through valve V and into the film. After flow through the channel, the solution is collected at the lower reservoir RB and returns to the top one via pump P. An over-flow pipe OF is install in the top reservoir to keep the solution level there fixed. We isolate the film from ambient air by gluing a plastic plate on the back of the channel. The plastic plate SP on the front is attached to sliding tracks ST, giving one access to make a soap film after the film ruptures. There are several ways to generate turbulence in this channel. If the comb is present, turbulence created by fluid rushing through the comb's teeth is dominated by enstrophy cascade, with an energy spectrum scaling $E(k) \sim k^{-3}$. If the comb is not present and the walls are not smooth, turbulence is generated by the rough walls and is dominated inverse energy cascade: $E(k) \sim k^{-5/3}$.

Experimental studies of 2D turbulence appeared much later after a number of theoretical predictions had been made. One of the first attempts was done by Couder [69, 2] in a horizontal soap film. The film was created by dipping a rectangular frame into a soapy solution and then setting the frame in a horizontal position. A comb made of an array of circular cylinders was used to pierce the film, and moved with a velocity ranging from 5 cm/s to 60 cm/s. Then, streets of vortices appeared behind the cylinders. Interactions between these vortices formed the so-called "decaying turbulence" because energy was only injected into the flow at the moving comb. Couder made no attempt to characterize this type of turbulence.

In a different experimental setup, in which a soapy solution flowed down vertically between two parallel wires under gravitational force, Kellay [66] inserted a comb in the flow to produce turbulence. The fluid rushing through the comb also resulted in decaying turbulence as in the experiment by Couder, but with a much higher range of Reynolds numbers. This is the original design from which subsequent experiments in soap-film channels [52, 33, 65, 50, 36, 51] including ours [40, 41] are based on. The energy spectrum $E(k)$ measured in this experiment has a power law $E(k) \propto k^{-3.3}$ and is in accord with the idea of an enstrophy cascade. There was no evidence of an inverse energy cascade in this turbulent flow. This may be explained by the lack of continuous feeding of energy into the flow: vortices injected at the comb are not replenished as the fluid moves downstream.

In an effort to create an inverse energy cascade turbulence in soap film, Rivera [73] used magnetic field to drive fluid motion in soap film that had been made electrolytically conducting by the addition of dissolved salt. (This method had been employed earlier in stratified fluid layers experiments [72, 74].) The magnetic field was varied spatially by placing horizontal arrays of rare earth magnets underneath a horizontal soap film. The magnets were positioned so that the magnetic field was perpendicular to the film. The frame that hanged the soap film was a rectangular one having two opposite sides made of stainless steel; the other two sides were made of plastic. Since the soapy solution was electrolytic, a voltage difference between the stainless steel sides caused a current of charges. The resultant Lorentz forces acting on charged fluid elements then drove the flow to turbulent state. Thus in this experiments, energy was continuously injected into the fluid, transfered to larger scales through a vortex-merging process, and eventually dissipated by air drag; the inverse energy cascade was formed. The presence of the enstrophy cascade was not reported in this study.

An evidence of the coexistence of an inverse energy cascade and an enstrophy cascade was first reported by Rutgers [33]. In this study, turbulence in a vertical soap-film channel was generated by inserting slanted combs into the flowing film. Each comb's orientation made a small angle with the vertical direction, allowing small vortices produced by its teeth to be swept into the mean flow. These vortices provided a constant flux of energy at roughly one length scale comparable to the comb's tooth size, and accordingly gave rise to a cascade of energy to larger length scales (i.e., an inverse energy cascade). At the same time, a cascade of enstrophy from the injection length scale to smaller length scales was also recorded in the turbulent energy spectrum. The enstrophy cascade was shown to cover a large range of length scales while the inverse energy cascade only covered a fraction of a decade. This limitation is probably due to the limited width of the channel, which dictates the largest length scale of energy dissipation.

Of all the above-mentioned experiments, turbulence was either created by putting obstacles to disturbed a fluid flow, or by applying external forces. In this study, we propose a novel way to create turbulence using rough boundaries in the modified soap film channel described in section 5.2. The smooth blades supporting the film can be replaced by blades with curved edges (Fig. 5.3) (or most simply by band saw blades). A 2D rough wall channel built this way is capable of sustaining steady-state turbulent flows. In these flows, the energy spectrum measured far from the boundary typically has a power law with exponent $-5/3$ for roughly one decade in wavenumber. One can enhance spectral homogeneity in the horizontal direction by inserting a rod at the end of the expansion section. The von-Karman wakes induced by the rod help carrying small vortices created near the rough walls to the mean flow. Replacing the rod by a comb generates decaying turbulence (with scaling exponent -3) which completely suppress turbulence coming from the wall (with scaling exponent $-5/3$). In either case, with or without the comb, the energy spectrum does not show the coexistence of an inverse energy cascade and an enstrophy cascade.

5.4 Experimental techniques

5.4.1 Flow visualization: Optical interference

Flow visualization is an important tool in fluid dynamics problems. For soap-film flows, optical interference is a natural choice among many other flow visualization methods because of its simplicity and intuitive interpretation.

When a soap film is illuminated by a monochromatic lamp, reflected light on the film surfaces interferes constructively or destructively with the incident light to form interference fringes consisting of bright and dark lines, respectively (Fig. 5.4a). For a given wavelength of the light, the film thickness dictates the interference condition, so that the thickness of the film is constant along a fringe. The change in thickness between any two successive fringes is a fraction of the wavelength of the light. If there is no obstacle in the film flow, the flow is laminar and the the fringes can be observed with ease (Fig. 5.4a).

If the flow is made turbulent, its thickness fluctuates so fast that it is not possible to distinguish between dark and bright fringes and the film looks gray. A fast camera is then used to capture the interference pattern in a small time interval. In our experiment, we used a high speed camera (Phantom V5.0, Vision Research Inc.) that is capable capturing images in a fraction of a second ($\sim 10\,\mu$s). The monochromatic light source is a sodium lamp producing yellow light at 589.3 nm wavelength. The results are shown in Fig. 5.4b. Here, small changes in thickness reflect small changes in the absolute value of the instantaneous velocity of the flow, so the figure can be interpreted as a map of the instantaneous spatial distribution of turbulent fluctuations downstream of the comb.

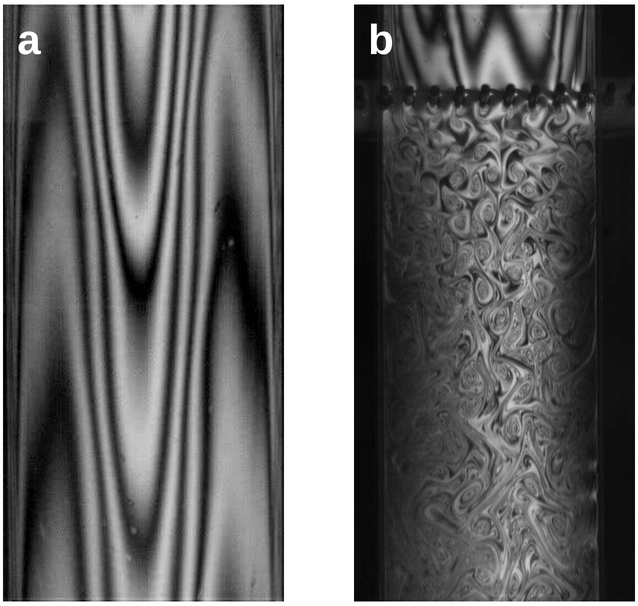

Figure 5.4: Interference fringes observed on the film in yellow light ($\sim$ 600 nm). **(a)** Soap film flow in a smooth channel without a comb. **(b)** Soap film flow in a smooth channel with a comb.

5.4.2 Measuring film thickness: Dye method

The thickness of a soap film can be measured by mixing the soapy solution with a dye such as Fluorescein (Sigma Chemical Co.). Where a blue (488 nm in wavelength) laser beam impinges on surface of the film, the dyed solution emits light in the yellow (518 nm in wavelength). If the soap-film flow is in steady state, the intensity measured at one point over a time interval Δt is readily detectable with an avalanche photodiode and is proportional to the time-averaged thickness of the film at that point.

If the fluorescent soapy solution is also mixed with small particles that scatter light, one can at the same time measure both the flow velocity u (using Laser Doppler Velocimetry (LDV) [75]) and the thickness h. The experimental setup to carry out these measurements is shown in Fig. 5.5. The LDV has two laser beams tightly focused on a small cylindrical volume of the film where the velocities of the particles passing through are being recorded. This cylindrical volume is called the scattering volume; it has a diameter of roughly 20μm (the diameter of the laser beams) and the same thickness as the film. In the steady state, the velocities fluctuate around a stationary mean value, which is the time-averaged velocity at that point, with standard deviations of a few percents of the mean velocity. Light emitting from the dye in the scattering volume falls on one end of a multi-mode optical fiber (OZ optics Ltd.) connecting to an avalanche photodiode (PerkinElmer Single Photon Counting Module). The fiber is positioned at an angle with the LDV laser beam to avoid direct light from the laser. The intensity of scattering light recorded by the photodiode at a horizontal position y is proportional to the film thickness and is denoted $\tilde{h}(y) = C_h h(y)$, where C_h is the conversion coefficient and $h(y)$ is the film thickness in micrometers. By putting the laser source and the photodiode on a translation stage which can move horizontally across the width of the film, one can obtain the relative thickness and velocity profiles of the film at a certain vertical position.

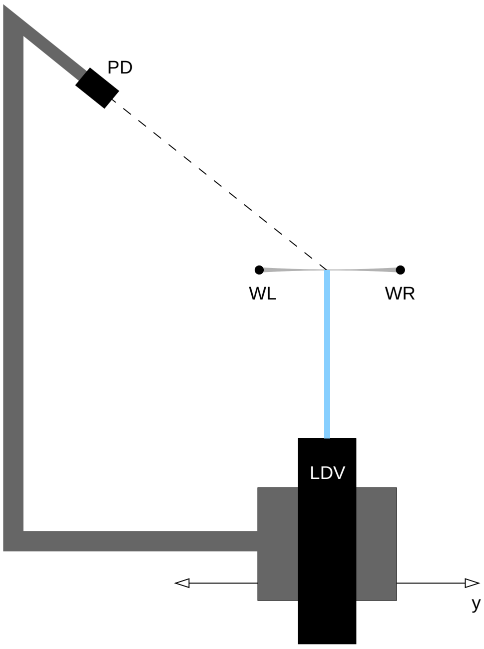

Figure 5.5: Top view of the experimental setup to measure thickness and velocity profiles of a soap-film flow. The soap film is supported by two wires WL and WR. The LDV is mounted on a translation stage that can move in the horizontal direction The two laser beams of the LDV focus on a small area of $20\,\mu$m in diameter on the film and measure the time-averaged velocity of the flow there. A photodiode PD is aimed to the illuminated area; the intensity I recorded by the photodiode is proportional to the film thickness. By attaching the photodiode to an arm connected to the translation stage, it can move along with the LDV, making it possible to carry out measurements of the thickness profile. Figure is not shown to exact scale.

Once the velocity profile $u(y)$ and the thickness profile in relative units $\tilde{h}(y)$ have been measured, it is possible to calibrate the absolute film thickness $h(y)$ by solving for the conversion coefficient C_h. Note that the volumetric flux Q, which is measurable, is calculated as follows:

$$
\begin{aligned}
Q = \int_0^w u(y)h(y)dy = C_h \int_0^w u(y)\tilde{h}(y)dy, \\
\Rightarrow C_h = \frac{Q}{\int_0^w u(y)\tilde{h}(y)dy}
\end{aligned}
\tag{5.1}
$$

where w is the film width. Thus the film thickness profile in absolute units is given by the expression, $h(y) = \tilde{h}(y)/C_h$.

In Fig. 5.6, we show thickness and velocity profiles of a soap film flow measured simultaneously.

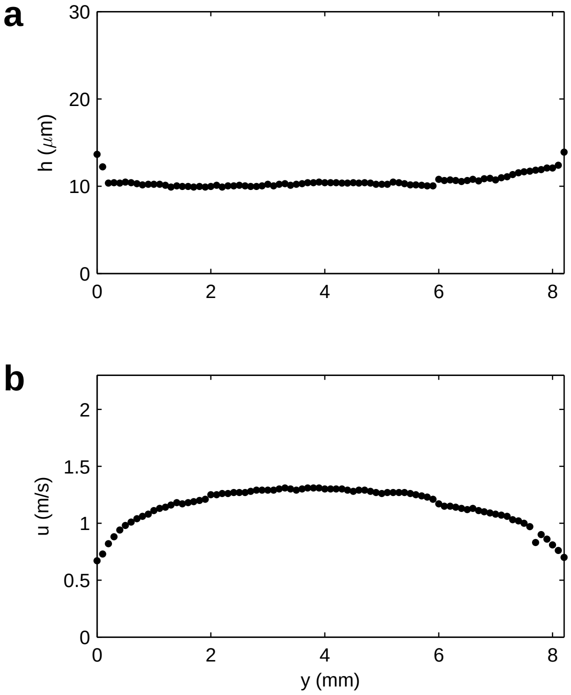

Figure 5.6: Velocity and thickness profiles measured simultaneously.

5.4.3 Measuring velocity: Laser Doppler Velocimetry

Laser Doppler Velocimetry (LDV) is probably the most common method for measuring the velocity of fluid flows. Since the technique is well documented in literature [75], we will only present a brief description of the method. In principle, the scheme allows one to measured two velocity components in a small measurement volume. The fluid has to be seeded with particles of diameter smaller than the film thickness and roughly the same mass density as that of the fluid.

We use particles manufactured by Esprix Technologies. The particles have a density only 5% higher than the density of the soapy solution and are small enough ($\sim 0.4\ \mu$m in diameter) to follow the fluid velocity. The measurement volume is the intersection of two laser beams splited from a laser source (Innova 90, Coherent Inc.). The intersection is usually a prolate ellipsoid with a minor diameter of $20\,\mu$m and a length of a few millimeters. Light scattered from particles passing through the measurement volume is recorded by a photon detector to measure the Doppler frequency shift, hence the velocities of particles.

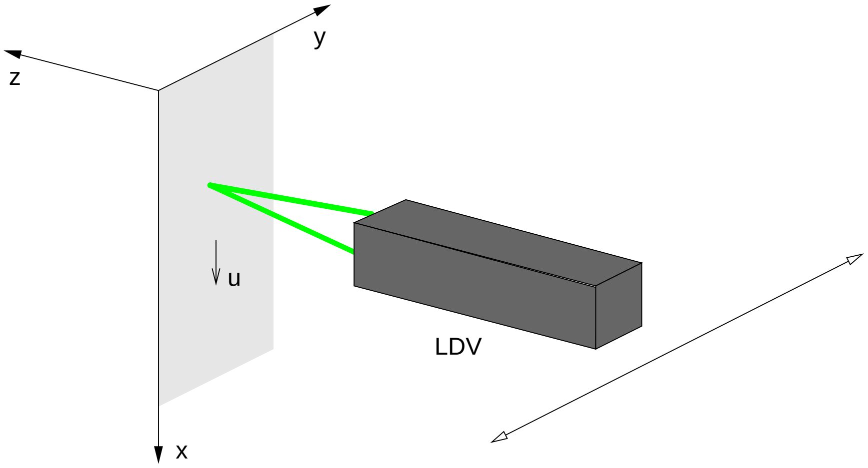

Figure 5.7: Using LDV to measure the fluid velocity in soap film flows.

In our LDV system, manufactured by TSI Inc., the photon detector is designed to receive back-scattered light by putting it in the same probe that emits two laser beams. (Fig. 5.7). On the one hand, this design offers great flexibility and help to protect the detector from direct laser light. On the other hand, light reflected from the film surface can be directly pointed back to the photo detector, hence overwhelming Doppler signals and causing saturation in the detector. One can avoid the reflected light by shielding it from or letting it bypass the LDV collection optics.

5.4.4 Positioning devices and synchronization

Automated positioning devices are very powerful tools in obtaining reproducible results. In our experimental studies, we carry our measurements of velocity and thickness profiles along cross sections of a soap film. Such measurements require a sequence of moving the LDV by a small and exact distance followed by a halt of the LDV for a certain time interval to record data. For that purpose, we mount the LDV probe on a motorized translation stage driven by a motion controller (SMC 100CC, Newport Inc.). A LabView program was developed to send instructions to the controller and acquire the stage's velocity and position. A normal procedure to measure a horizontal velocity profile can be described as a sequence of identical steps. In each step, the motion controller is instructed to move the LDV for a distance Δy, then the LDV starts collecting data until a certain time interval Δt has elapsed.

The motorized positioning device can also be synchronizes with the LDV program to automatically obtain velocity profiles in the horizontal direction. Data taken by the LDV is in the form of a series of velocity $u_i = u(t_i)$ of particle passing through the measurement volume at time t_i. Note that there is only one particle velocity recorded at a time. The length of this time series is usually 1 million and the recording time is few minutes depending on the data rate. The time series can be divided into smaller series corresponding to different spatial position of the LDV, given that one can keep track of the time the LDV changes its state from halting to moving or vice versa. The LDV processor allows one to reset the time series's reference to zero whenever a rising logic level (+5V) is sent to the LDV processing module. The signal is sent through a Multifunction Data Acquisition card (NI PCI-MIO-16XE-10). We have developed a LabView program to synchronize the LDV's reseting time and its motion, that is, whenever the motion controller is instructed to move or stop the LDV, a 5V logic level is sent to the LDV processor to reset the time stamp.

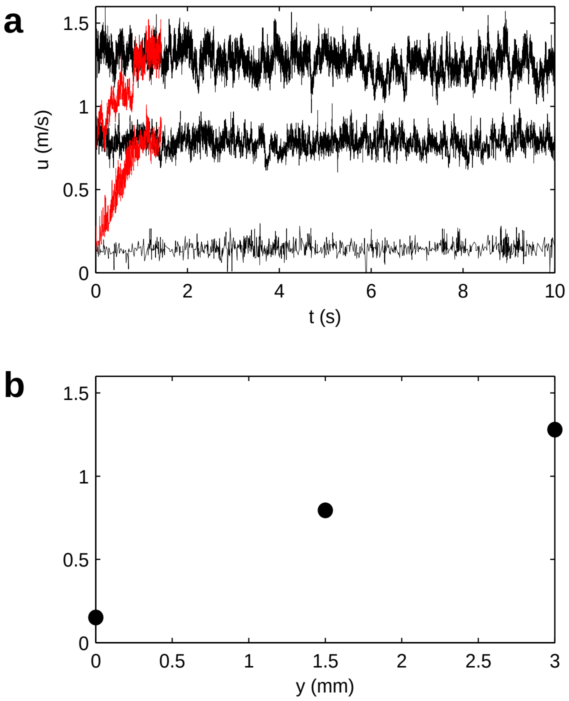

Figure 5.8: **(a)** Time series of velocity of a soap film flow recorded by the LDV with the time reference is reset whenever the translation stage is instructed to change its state from moving to halting or vice versa. The black and red colors indicate the data recorded when the LDV halts and moves respectively. **(b)** Time averaged velocity extracted from the measurement in **b**: three points correspond to data acquired at three spatial position when the LDV is not moving.

5.4.5 Errors in the measurement of friction factor

The dominant sources of errors in the measurements of the friction factor arise from the uncontrolled conditions in the experiments. There are two major sources of these uncontrolled conditions: (1) the variations in the flow speed through the valve V, and (2) the out-of-plane motion of the film induced by the velocity fluctuations in the surrounding air. (The velocity fluctuations could be only partially suppressed by placing the entire apparatus in a tent.) Next we discuss how we estimate the errors induced by these uncontrolled conditions of the experiment.

In order to estimate the error of friction factor, we need to estimate the errors in the measurement of the velocity and the velocity gradient (please refer to chapter 4 for more details). To estimate the error in measuring the velocity, we keep the experimental conditions constant and make repeated measurements of time-averaged velocity at a fixed point on the film. We find that the average changes less than 5% amongst the different measurements. Thus, we estimate the upper bound of error in velocity measurement as $\delta U/U \approx 5\%$. The velocity gradient close to the wall G is estimated by applying a linear fit to the velocity profile close to the wall. The root mean square error of the fit is typically smaller than 5%. Thus, we estimate the upper bound of error in velocity gradient as $\delta G/G \approx 5\%$. The upper bound of error of friction factor δf can be expressed as:

$$\begin{aligned}
\delta f &= \left|\delta\left(\nu\frac{G}{U^2}\right)\right| = \nu\left|\frac{\delta G}{U^2} - \frac{2U\delta UG}{U^4}\right| = \nu\left|\frac{\delta G}{G}\frac{G}{U^2} - 2\frac{\delta U}{U}\frac{G}{U^2}\right| \\
\Rightarrow \delta f &\leq \nu\left(5\% \times \frac{G}{U^2} + 2 \times 5\% \times \frac{G}{U^2}\right) = 15\% f \\
\Rightarrow \frac{\delta f}{f} &\leq 15\%. \qquad (5.2)
\end{aligned}$$

Thus, we conclude that the errors in the measurement of the friction factor is less than 15%, which is comparable to the scatter of the data in Fig. 4.5.

Chapter 6

Conclusions and future work

We have verified experimentally that the functional relation between the frictional drag and the Reynolds number of a turbulent soap-film flow on smooth walls is set by the type of turbulent spectrum that prevails in the flow. For soap-film flows with the type of spectrum known as the enstrophy cascade (for which the spectral exponent equals 3), we have found that the frictional drag scales as $\mathrm{Re}^{-1/2}$. For soap-film flows with the type of spectrum known as the inverse energy cascade (for which the spectral exponent equals 5/3), we have found that the frictional drag scales as $\mathrm{Re}^{-1/4}$. These scalings are in accord with the prediction of a recently proposed spectral theory of the frictional drag [15, 1, 26, 27, 28, 29, 30]. According to this theory, the frictional drag of turbulent soap-film flows on smooth walls should scale in the form, $f \propto \mathrm{Re}^{\beta}$, where β, the generalized Blasius exponent, is set by the spectral exponent α and can be computed using the expression $\beta = (1-\alpha)/(1+\alpha)$.

Our experimental results evince, and the spectral theory predicts, the existence of a "spectral link" between the frictional drag of the flow and the statistical structure of the turbulent fluctuations in the flow. As per this spectral link, the familiar empirical exponent of Blasius ($-1/4$) is but as a direct macroscopic manifestation of the statistical structure of the turbulent fluctuations in the flow, and can be expressed as a recast form of of the spectral exponent of Kolmogorov ($\alpha = 5/3$). If the nature of the turbulent fluctuations changes, and the spectral exponent changes accordingly, then the familiar empirical exponent of Blasius will not obtain: the generalized Blasius exponent will obtain instead, and its value will be set by the changed value of the spectral exponent.

The existence of a spectral link cannot be reconciled with the classic Prandtl theory of the frictional drag. In this theory we are provided with no means of distinguishing between one type of turbulent spectrum and another. Thus, the classic theory is constitutionally incapable of accounting for a spectral link. In view of our experimental results, the theory must be considered incomplete.

It is interesting to recall that the classic theory of the frictional drag follows from the log law of the wall [60]. If the log law of the wall were the case in all pipe flows regardless of the type of spectrum, there is no doubt that the frictional drag would be independent of the type of spectrum. There would be no spectral link.

Note, however, that the log law of the wall is predicated on general arguments of similarity. These arguments are mathematical in nature; they hardly include any physics; and they make no reference to the turbulent spectrum (or, in general, to the statistical structure of the turbulent fluctuations in the flow). As the spectrum is excluded from consideration a priori, it cannot come as a suprise that the classic theory fails to predict a spectral link. Further, in view of our experimental results, it is apparent that the log law of the wall is unlikely to be valid irrespective of the type of spectrum. There is a need for a spectral theory of the turbulent mean velocity profile.

In the spectral theory of the frictional drag, the revolving velocity of an eddy of any given size is determined from the turbulent spectrum. This provides the spectral link. The shear stress at the wall arises from the transfer of momemtum effected by the eddies that are present close to the wall [1, 26]. Thus, according to the spectral theory, the frictional drag is a local phenomenon, and it can be affected by remote conditions only to the extent that the turbulent spectrum that prevails locally may be affected by remote conditions.

This prediction of the spectral theory is consistent with our experimental results on soap-film flows. Consider, for example, our experiments in soap-film flows with the inverse energy cascade. As noted earlier, we believe to have been the first to have realized a soap-film flow with a pure inverse energy cascade. We have shown that a pure inverse energy cascade can be induced by making one of the walls of the soap-film channel rough. The effect of the rough wall extended over the entire soap-film channel, and the spectrum close to the other wall, which remained smooth, was the inverse energy cascade. In accord with the prediction of the spectral theory, the frictional drag measured at the smooth wall was the Blasius scaling. Thus, the remote (as seen from the smooth wall) rough wall had no effect on the frictional drag at the smooth wall—except through the turbulent spectrum that prevailed close to the smooth wall.

In our experiments, many of the soap-film flows extended for more than 1 m downstream, and we discovered that in such flows there forms a new type of shock that stems form the elasticity of the film. This discovery had an impact on our work on the frictional drag: it allowed us to perform both slow-flow and fast-flow measurememts in a single soap film. We have developed a theoretical explanation of these "Marangoni shocks," and compared the theoretical predictions with experimental measurements.

Looking to the future, further research on the spectral link and the frictional drag should concern the Strickler regime of fixed roughness and high Reynolds number. The spectral theory can be used to make a specific prediction as to the scaling of f with the relative (dimensionless) roughness; the result is a generalized Strickler scaling in which the exponent is set by the spectral exponent. This prediction should be tested experimentally, and we have carried out some preliminary work to this effect. We have made a soap-film channel in which both walls are rough, and we have been able to measure the Reynolds shear stress and the viscous stress along the wetted surface tangent to the roughness elements, using Particle Image Velocimetry. The preliminary results are encouraging, but we have not been able to reach a high enough Reynolds number to attain independence of the frictional drag on the Reynolds number. The highest Reynolds number that can be attain at present is about 120,000.

In order to obtained soap-film flows with higher Reynolds number, we need to overcome a number of difficulties. First of all, since the flow is driven by gravity, a longer channel is needed to give the fluid enough time to accelerate. Since film ruptures would happen easily due to disturbances from the air at high velocity, the film should be better isolated, while easy access is still required to rebuild a film after it ruptures. In addition to that, any imperfect alignment between two blades is likely to cause film rupture, and should be eliminated at all cost.

Appendix A

One-dimensional model of falling soap film

Here we discuss three topics pertaining to the one-dimensional (1D) model of falling soap film employed in Chapter 2. First, starting with the Navier–Stokes equations, we derive the equation of momentum balance, $\rho h u u_x = 2\sigma_x + \rho g h - 2\tau_a$ (equation (2.1)). Then we discuss the modeling of two terms of this equation: the surface tension gradient term (σ_x) and the air friction term (τ_a, equation (2.2)).

A.1 Equation of momentum balance

A.1.1 Governing equations and boundary conditions

In this section we will derive the governing equations and the boundary conditions for a thin sheet of liquid falling under gravitational force, as shown in Fig. A.1.

The vertical and horizontal axes are denoted x and y, respectively. The film flow is driven by gravity, which is directed along the x-axis. We assume that the film is extended infinitely in the z direction, although in an actual setup, the film's dimension in this direction is varied between 0.5 cm to 5 cm. This assumption is based on the actual dimensions of the soap films used in our experiments: the thickness of these films (in y direction) is of order $1\,\mu$m, while their width (in z direction) is of order 1cm; thus, the width is three orders of magnitude larger than the thickness. We also assume that the two film surfaces are symmetric with respect to the x-axis and have elevations $y = \pm h_1(x,t)$. The thickness of the film is therefore $h(x,t) = 2h_1(x,t)$. The interstitial fluid moves with a two-dimensional

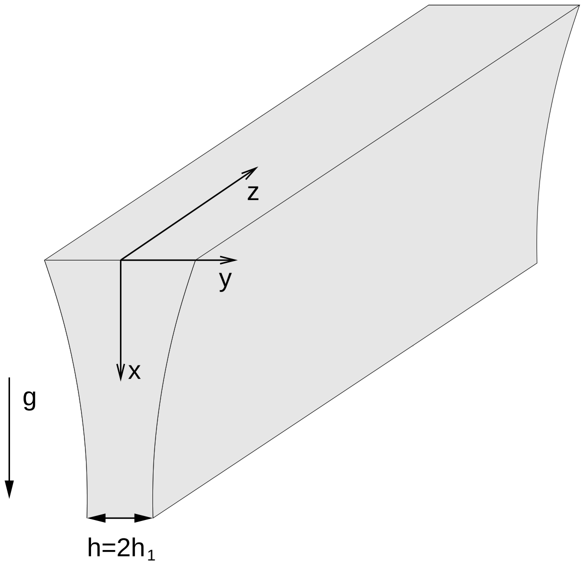

Figure A.1: A thin liquid sheet falling under gravitational force. The flow is in the x direction. The sheet is assumed to extend infinitely in the z direction and symmetric across the (x, z) plane.

velocity distribution $\mathbf{u} = (u, v)$, with $u(x, y, t)$ and $v(x, y, t)$ being the vertical and horizontal components, respectively. The fluid is incompressible with density ρ and viscosity $\nu = \mu/\rho$, both of which are independent of the amount of soap. The pressure inside the film is $p(x, y, t)$. There are soap molecules in the bulk with volumetric concentration c_b and on the two surfaces with surface concentration Γ. The resultant surface tension σ is different from that of water σ_0 due to the presence of soap molecules. The gravitational acceleration is $\mathbf{g} = (g, 0)$. The governing equations for the fluid are the incompressible Navier-Stokes equations:

$$\nabla \cdot \mathbf{u} = 0, \tag{A.1}$$

$$\rho \frac{D\mathbf{u}}{Dt} = -\nabla p + \mu \nabla^2 \mathbf{u} + \rho \mathbf{g}. \tag{A.2}$$

In the above equation, we use the substantial derivative D/Dt:

$$\frac{D}{Dt} = \frac{\partial}{\partial t} + \mathbf{u} \cdot \nabla. \tag{A.3}$$

Equation (A.1) is the continuity equation and represents the fluid's incompressibility. Equation (A.2) describes the conservation of momentum. The different terms in this equation, starting from the left end, represent the effects of inertia, pressure gradient, viscosity, and gravity.

In order to have a complete description of the film, we have to specify its boundary conditions. Because of the assumed symmetry, it is not necessary to write the boundary condition at both surfaces of the film. Hence, in what follows, we only derive the conditions for one surface of the film.

First, consider a film surface with elevation $h_1(x,t) = h(x,t)/2$ and curvature $\kappa(x,t)$. The normal vector to the film surface, $\mathbf{n}$, is directed outward of the fluid and the tangent vector, $\mathbf{t}$, is directed along with the vector denoting the fluid velocity at the film surface. The surface vectors and curvature can be calculated as follows:

$$\mathbf{n} = \frac{1}{(1+h_{1x}^2)^{1/2}}(-h_{1x}, 1), \tag{A.4}$$

$$\mathbf{t} = \frac{1}{(1+h_{1x}^2)^{1/2}}(1, h_{1x}), \tag{A.5}$$

$$\kappa = \frac{h_{1xx}}{(1+h_{1x}^2)^{3/2}}. \tag{A.6}$$

Let us denote the stress tensor of the interstitial fluid as $\boldsymbol{\tau}$. It can be used to calculate the force $\mathbf{f}$ that acts on a surface with normal vector $\mathbf{n}_i$:

$$\mathbf{f} = \boldsymbol{\tau} \cdot \mathbf{n}_i. \tag{A.7}$$

Also, using the deformation law, the stress tensors can be expressed in terms of the pressure and velocity fields in the bulk fluid:

$$\boldsymbol{\tau} = -p\mathbf{I} + \mu(\nabla \mathbf{u} + \nabla \mathbf{u}^T). \tag{A.8}$$

Substitution of equation (A.8) into equation (A.7) gives the force acting on an arbitrary surface in the bulk:

$$\mathbf{f} = -p\mathbf{n}_i + \mu(\nabla\mathbf{u} + \nabla\mathbf{u}^T) \cdot \mathbf{n}_i. \tag{A.9}$$

Since the above equation holds for any surface in the bulk fluid, it is also true for the film surface, which has normal vector $\mathbf{n}$:

$$\mathbf{f} = -p\mathbf{n} + \mu(\nabla\mathbf{u} + \nabla\mathbf{u}^T) \cdot \mathbf{n}. \tag{A.10}$$

To obtain the dynamic boundary condition, consider a fluid element on the film surface, which element is subject to the force from the ambient air, surface tension and the force from the interstitial fluid. The force that the ambient air applies on this fluid element is

$$\mathbf{f}_a = -p_a\mathbf{n} - \tau_a\mathbf{t}, \tag{A.11}$$

where $-p_a\mathbf{n}$ is the atmospheric pressure, $-\tau_a\mathbf{t}$ is the frictional force per unit area that the ambient air acts on the film surface. Also, the surface tension can be written as $\kappa\sigma\mathbf{n} + \nabla_s\sigma$, where $\nabla_s = \nabla - \mathbf{n}(\mathbf{n} \cdot \nabla)$ is the surface gradient operator. Thus, the force balance equation for the film surface is:

$$-\mathbf{f} + \mathbf{f}_a + \kappa\sigma\mathbf{n} + \nabla_s\sigma = 0. \tag{A.12}$$

On rearrangement, we obtain the dynamic boundary condition at $y = h_1$:

$$-(p - p_a)\mathbf{n} + \mu(\nabla\mathbf{u} + \nabla\mathbf{u}^T) \cdot \mathbf{n} + \tau_a\mathbf{t} = \kappa\sigma\mathbf{n} + \nabla_s\sigma. \tag{A.13}$$

Equation (A.13) can be projected on the surface's normal vector by multiplying both sides with $\mathbf{n}$:

$$-(p - p_a) + \mathbf{n} \cdot \mu(\nabla \mathbf{u} + \nabla \mathbf{u}^T) \cdot \mathbf{n} = \kappa\sigma, \tag{A.14}$$

The projection of equation (A.13) on the surface's tangent vector gives another condition:

$$\mathbf{t} \cdot \mu(\nabla \mathbf{u} + \nabla \mathbf{u}^T) \cdot \mathbf{n} + \tau_a = \mathbf{t} \cdot \nabla_s \sigma, \tag{A.15}$$

The kinematic boundary condition at $y = h_1$ reads:

$$v = \frac{Dh_1}{Dt}. \tag{A.16}$$

The fluid motion of the film is thus described by the equations (A.1), (A.2), and the boundary conditions (A.14), (A.15), (A.16). Yet these equations are not complete because models for surface tension σ and air drag τ_a are not specified. These models are discussed in sections A.2 and A.3. For now let us proceed to the nondimensionalization of the governing equations and boundary conditions.

A.1.2 Nondimensionalization

The soap film has a typical length L and an average thickness H. The typical velocity in vertical and horizontal directions are denoted U and V, respectively. The pressure in the fluid is assumed to fluctuate around the atmospheric pressure p_a with amplitude $\mu U/L$. The same assumption is applied to surface tension. Also, we introduce a small dimensionless parameter $\epsilon = H/L \ll 1$. Based on these assumptions the dimensionless variables, denoted with primes, are related to the dimensional ones as follows:

$$\begin{aligned} x &= Lx', & y &= Hy' = \epsilon Ly', \\ u &= Uu', & v &= Vv' = \epsilon Uv', \\ h_1 &= Hh_1', & t &= \frac{L}{U}t', \\ p &= p_a + \frac{\mu U}{L}p', & \sigma &= \gamma + \Delta\gamma\sigma'. \end{aligned} \tag{A.17}$$

On substitution of these new variables into the governing equations and the boundary conditions, the following parameters are introduced:

- The Reynolds number $\mathrm{Re} = \frac{UL}{\nu}$: a dimensionless number that characterizes the relation between inertia and viscous effect.
- The Froude number $\mathrm{Fr} = \frac{U^2}{gL}$: a dimensionless number comparing inertia and gravitational force.
- The Capilliary number $\mathrm{Ca} = \frac{\mu U}{\gamma}$ compares viscous force and surface tension.
- The Marangoni number $\mathrm{Ma} = \frac{\Delta\gamma}{\mu U}$ is defined as the ratio between surface tension force and viscous effect.

Substituting these new variables into the governing equation and write them in scalar form, after dropping primes, we have:

$$u_x + v_y = 0, \tag{A.18}$$

$$\epsilon^2 \mathrm{Re} \frac{Du}{Dt} = -\epsilon^2 \frac{\partial p}{\partial x} + \epsilon^2 \frac{\partial^2 u}{\partial x^2} + \frac{\partial^2 u}{\partial y^2} + \epsilon^2 \frac{\mathrm{Re}}{\mathrm{Fr}}, \tag{A.19}$$

$$\epsilon^2 \mathrm{Re} \frac{Dv}{Dt} = -\frac{\partial p}{\partial y} + \epsilon^2 \frac{\partial^2 v}{\partial x^2} + \frac{\partial^2 v}{\partial y^2}. \tag{A.20}$$

Similarly, the dynamic boundary conditions at $y = h_1$ are:

$$p + \epsilon \left(\frac{1}{\text{Ca}} + \text{Ma}\sigma \right) \frac{h_{1xx}}{(1 + \epsilon^2 h_{1x}^2)^{3/2}} = \frac{2}{1 + \epsilon^2 h_{1x}^2} (\epsilon^2 u_x h_{1x}^2 - \epsilon^2 v_x h_{1x} - u_y h_{1x} + v_y), \tag{A.21}$$

$$\epsilon \text{Ma} \sigma_x = \frac{1}{1 + \epsilon^2 h_{1x}^2} \left[2\epsilon^2 h_{1x}(v_y - u_x) + (1 - \epsilon^2 h_{1x}^2)(u_y + \epsilon^2 v_x) + \epsilon \frac{L}{\mu U} \tau_a \right]. \tag{A.22}$$

The kinematic boundary condition at $y = h_1$ is:

$$v = \frac{Dh_1}{Dt}. \tag{A.23}$$

A similar set of boundary conditions for the opposite surface $y = -h_1$ can be written to complete the system of equations describing the film flow. Alternatively, we can use the symmetric assumption of the film geometry and replace the condition at $y = -h_1$ by the following condition at $y = 0$:

$$\begin{aligned} v &= 0, \\ u_y &= 0. \end{aligned} \tag{A.24}$$

A.1.3 Asymptotic expansion

The system of equations describing the film behavior is complicated and cannot be solved analytically. It is, however, possible to approximate the solutions by using asymptotic expansions. An asymptotic expansion requires estimates of parameters in the governing equations. In our soap-film channel, the Reynolds number is roughly 10^4, while $\epsilon = H/L \approx 10^{-5}$ (See table A.1). Hence, we assume that $\text{Re} = \mathcal{O}(\epsilon^{-1})$. We choose to include the Marangoni and surface tension effects in the system by setting $\text{Ca} = \text{Ma} = \mathcal{O}(1)$. In this limit, the solution of velocity field and pressure can be expanded in power series of the small parameters ϵ as follows:

$$(u, v, p) = (u_0, v_0, p_0) + \epsilon(u_1, v_1, p_1) + \epsilon^2(u_2, v_2, p_2) + \cdots . \tag{A.25}$$

Parameters	**Symbol**	**Estimate**
Viscosity of soap solution	μ	$\approx 10^{-3}\,\mathrm{kg/(m\ s)}$
Density of soap solution	ρ	$\approx 1000\,\mathrm{kg/(m^3)}$
Kinematic viscosity	ν	$\approx 10^{-6}\,\mathrm{m^2/s}$
Characteristic quantities		
Film length	L	$\approx 1\,\mathrm{m}$
Average film thickness	H	$\approx 10^{-5}\,\mathrm{m}$
Mean velocity	U	$\approx 1\,\mathrm{m/s}$
Dimensionless numbers		
	ϵ	10^{-5}
Reynolds number	Re	10^4
Froude number	Fr	10^{-1}
Capilliary number	Ca	10^{-2}

Table A.1: Estimates of parameters and characteristic quantities of soap-film flows.

Leading-order equations

On substitution of the power series of velocity components and pressure into the governing equations and boundary condition, we obtain the zero-order equations:

$$u_{0x} + v_{0y} = 0, \tag{A.26}$$

$$u_{0yy} = 0, \tag{A.27}$$

$$-p_{0y} + u_{0yy} = 0. \tag{A.28}$$

At $y = 0$, the velocity has to satisfy:

$$\begin{aligned} u_{0y} &= 0, \\ v_0 &= 0. \end{aligned} \tag{A.29}$$

The conditions at the surface $y = h_1$ become:

$$\begin{aligned} u_0 &= \frac{Dh_1}{Dt}, \\ p_0 &= -2u_{0y}h_{1x} + 2v_{0y}, \\ u_{0y} &= 0. \end{aligned} \tag{A.30}$$

The above system of equations can be simplified to the following:

$$\begin{aligned} u_0 &= u_0(x), \\ v_0 &= -u_{0x}y, \\ p_0 &= -2u_{0x}, \\ h_{1t} + (u_0h_1)_x &= 0. \end{aligned} \tag{A.31}$$

Hence the zero order solutions for u and p only depend on x and therefore are uniform across the thickness. The above set of equations is not sufficient to determine the velocity field, pressure and film thickness and should be completed by conditions specified by higher order expansions.

Next order

By collecting all the terms of order $\mathcal{O}(1)$ in the governing equations and boundary conditions, we have the first order system as follows:

$$
\begin{aligned}
u_{1x} + v_{1y} &= 0, && \text{(A.32)}\\
\epsilon \mathrm{Re} \frac{Du_0}{Dt} &= u_{1yy} + \epsilon \frac{\mathrm{Re}}{\mathrm{Fr}}, && \text{(A.33)}\\
0 &= p_{1y} + v_{1yy}. && \text{(A.34)}
\end{aligned}
$$

The boundary conditions at $y = 0$ are:

$$
\begin{aligned}
v_1 &= 0,\\
u_{1y} &= 0. && \text{(A.35)}
\end{aligned}
$$

The conditions at $y = h_1$ are:

$$
\begin{aligned}
p_1 + \left(\frac{1}{\mathrm{Ca}} + \mathrm{Ma}\sigma\right) h_{1xx} &= -2u_{1y}h_{1x} + v_{1y}, && \text{(A.36)}\\
\mathrm{Ma}\sigma_x &= u_{1y} + \frac{L}{\mu U}\tau_a. && \text{(A.37)}
\end{aligned}
$$

By integrating equation (A.33), in terms of y and applying the boundary condition (A.35), we have:

$$
u_{1y} = \epsilon \frac{\mathrm{Re}}{\mathrm{Fr}} y - \epsilon \mathrm{Re} \frac{Du_0}{Dt} y. \tag{A.38}
$$

Combine the above equation with the boundary condition at $y = h_1$, we have:

$$
u_{1y}\Big|_{y=h_1} = \epsilon \frac{\mathrm{Re}}{\mathrm{Fr}} h_1 - \epsilon \mathrm{Re} \frac{Du_0}{Dt} h_1 = \mathrm{Ma}\sigma_x - \frac{L}{\mu U}\tau_a. \tag{A.39}
$$

The final equations that govern the behavior of the thin film is:

$$\begin{aligned}\frac{\partial h_1}{\partial t} + \frac{\partial}{\partial x}(u_0 h_1) &= 0,\\ \epsilon \mathrm{Re} h_1 \frac{Du_0}{Dt} &= \epsilon \frac{\mathrm{Re}}{\mathrm{Fr}} h_1 - \mathrm{Ma}\sigma_x - \frac{L}{\mu U}\tau_a. \end{aligned} \tag{A.40}$$

In dimensional form, the above equations become:

$$\begin{aligned}\frac{\partial h_1}{\partial t} + \frac{\partial}{\partial x}(u h_1) &= 0,\\ \rho h_1 \frac{Du}{Dt} &= \sigma_x + \rho g h_1 - \tau_a. \end{aligned} \tag{A.41}$$

In a steady state we can write the above equations as:

$$\begin{aligned}\frac{\partial}{\partial x}(u h_1) &= 0,\\ \rho h_1 u u_x &= \sigma_x + \rho g h_1 - \tau_a. \end{aligned} \tag{A.42}$$

Note that $h_1 = h/2$. Thus the above equation can be rewritten in terms of h as:

$$\begin{aligned}\frac{\partial}{\partial x}(u h) &= 0,\\ \rho h u u_x &= 2\sigma_x + \rho g h - 2\tau_a. \end{aligned} \tag{A.43}$$

where the first equation is an expression of the incompressibility condition used in Chapter 2 ($uh = q$, where q is the constant flux per unit width of the film) and the second equation is the equation of momentum balance, equation (2.1).

A.2 Surface tension in soap films: Marangoni effect

In this section, a more detailed view of structure of soap film is presented. A soap film consists of two layers of soap molecules separated by a thin liquid layer [2]. In our experiments, the soap-film thickness ranges from fraction of a micron to 20 microns. The soap molecules, when added into water, tend to be distributed on the surface with their tails (hydrophilic) pointing outward and their heads (hydrophobic) in the water. These molecules cause the average distance between water molecules to be larger than it is in pure water. As a consequence, the surface tension forces between water molecules decrease. A lower surface tension is a crucial factor to help maintaining liquid film, since surface tension of water is too strong for the film to last for any length of time. Typically, surface tension of soap solution is a third of that of pure water.

Adding soap molecules in water not only reduces surface tension of water but also enhances the elasticity of the film. When a soap film is at equilibrium, the concentration of soap molecules on the surface has to take an optimum value to minimize surface energy. Any deformation of the film increases this surface energy. The energy minimization process results in a restoring force that opposes to the initial deformation. In this section, we shall seek an expression for this opposing force.

Denoting σ_0 and σ surface tensions of water and soap solution, respectively, we have the relation:

$$\sigma = \sigma_0 - f, \tag{A.44}$$

where f is called surface pressure caused by the soap molecules on the film surface. The equation governing the behavior of f is the Gibbs adsorption law:

$$df = RT\Gamma d(\ln \xi c_b), \tag{A.45}$$

where R is the gas constant, T is the temperature, Γ is the surface concentration. ξ is the activity coefficient, and c_b is the volumetric concentration of the interstitial fluid. In general, the relation between the surface and interstitial concentration is shown in Fig. A.2. It is

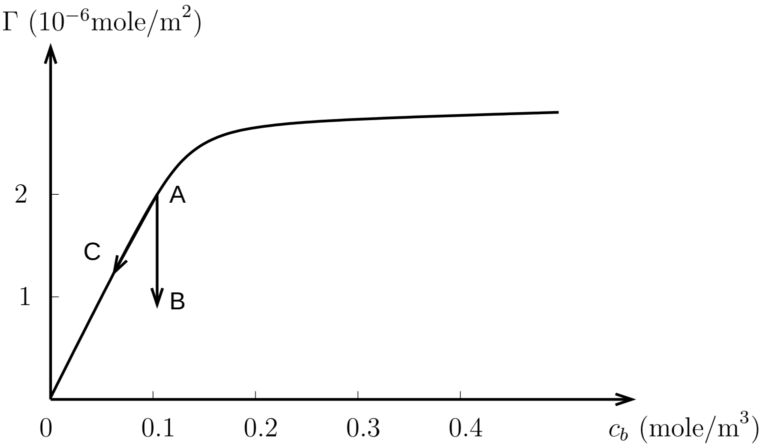

Figure A.2: The dependence of surface concentration Γ of soap molecules on the volumetric concentration c_b of the interstitial fluid. The path AB describes films in Marangoni regime: the surface concentration decreases due to compression or stretching of the surface; there is no soap molecules exchanged between the surface and the bulk. Path AC describes a film in Gibbs regime: the soap molecules have time to migrate between the surface and the bulk, hence Γ varies linearly with c_b. After [2].

clearly seen that the graph has two distinct regions separated by a sharp bend at $c_b = c_0$. For $c_b < c_0$, the surface concentration is linearly proportional to c_b:

$$\Gamma = kc_b, \tag{A.46}$$

where k is a property of the solution. In this small concentration range, the activity concentration $\xi = 1$, and the relation (A.45) can be integrated giving a simple expression for the surface pressure:

$$f = RT\Gamma. \tag{A.47}$$

As the concentration increases and pass a certain value c_0, called the critical micelles concentration (c.m.c), the relation between Γ and c_b is no longer linear. This is due to the fact that soap molecules start forming clusters, or micelles) in which their hydrophobic tails are isolated from water. The activity coefficient ξ is no longer unity and Γ increases very slowly with c_b. The dependence of surface pressure on concentration is then:

$$f = RT\Gamma_\infty \ln\left(1 + \frac{c_b}{a}\right), \tag{A.48}$$

where Γ_∞ and a are empirical constants.

All of our experiments are carried out using dilute soap solution, in which the relations between surface and bulk concentrations is always linear. In reality, when the film falls down freely, its surfaces maybe stretched or compressed. As a result, the energetically optimum state is disturbed, in which case the film responses in two possible ways:

- If the time scale of the deformation process is small compared to the time scale needed for soap molecules to migrate from the bulk to the surface, then there is no exchange of soap molecules between the bulk and the surface and the film is said to be in Marangoni regime. In this regime, the surface concentration change is solely due to surface area variation. The bulk concentration is kept constant. This process is illustrated by the path from A to B in Fig. A.2.

- If the time scale of the deformation process is larger than the time scale of the diffusion of soap molecules between the bulk and the surface, the film is said to be in Gibbs regime. In this case, the soap molecules have enough time to migrate from, or to, the surface. The relation between surface and bulk concentrations is therefore linear, as illustrated by the path from A to C in Fig. A.2.

It is worth noting that although surface deformation may alter surface concentration and consequently bulk concentration, the total concentration c is a constant and is related to the surface and bulk concentrations as follows:

$$c = c_b + \frac{2\Gamma}{h}. \tag{A.49}$$

Therefore, in Marangoni regime, the dependence of Γ on h can be expressed as the following:

$$\Gamma = \frac{(c - c_b)h}{2}, \tag{A.50}$$

where c and c_b are constants.

Determination of the relevant regime to the soap films in our experiments requires estimations of the time scale t_D for soap molecules to diffuse between the surface and the bulk and the time scale t_d of the deformation of a strip of soap film. Using the diffusion coefficient from [2] ($D = 4 \times 10^{-6}\,\mathrm{cm}^2/\mathrm{s}$), and for a film of thickness $h \approx 10\,\mu\mathrm{m}$, $t_D = h^2/D \approx 1\,\mathrm{s}$. For the deformation time scale, we can estimate its upper bound t_r by considering a horizontal strip of soap film falling down with a typical velocity $u = 1\,\mathrm{m/s}$ through a distance of typical value $L = 1\,\mathrm{m/s}$. The time for the strip to finish traveling the distance L is called the residence time and that can be approximated as t_r. Therefore $t_r = L/u = 1\,\mathrm{s}$. We conclude that $t_d \ll t_r \sim t_D$. This implies the films in our experiments are in Marangoni regime. On substitution of equation (A.50) into equation (A.47), we obtain the surface pressure f:

$$f = \frac{RT(c - c_b)h}{2}. \tag{A.51}$$

The surface tension gradient σ_x follows from equation (A.44):

$$\sigma_x = -f_x = -\frac{1}{2}RT\rho(c - c_b)h_x = -\frac{1}{2}\rho U_M^2 h_x, \tag{A.52}$$

where $U_M = \sqrt{RT(c - c_b)/\rho}$ is a constant independent of h. We use the above expression as a model for σ_x in equation (2.1).

In summary, we use low concentration soap solution in our experiments. The surface pressure is therefore linearly proportional to the surface concentration. At equilibrium, the relation between surface and bulk concentrations is linear. However, when the film undergoes a deformation process, as it falls down under gravity, there is no exchange of soap molecules between the bulk and the surface. The film's elasticity is said to be in Marangoni regime and the surface concentration is a linear function of the film thickness. The surface tension gradient is expressed by equation (A.52)

A.3 The air friction

A complete analysis for soap-film flows requires a model for frictional force cause by ambient air as a moving film unavoidably rubs against the surrounding air. In this section we present two simple models that have been used satisfactorily in previous studies to capture the effect of air friction.

Linear model of air friction

Consider an element of fluid moving in the air with velocity u. It experiences a drag force, due to the viscous stress of the surrounding air, which is proportional to its velocity and acts in the opposite direction:

$$\tau_a = -\alpha_a u, \tag{A.53}$$

where α_a is a constant. For soap film flows Rivera [73] determined $\alpha \approx 0.7$, although in some cases it can be treated as a free parameter.

Blasius model of air friction

Consider the thin film as a flat plate moving with velocity u. The drag force caused by the surrounding air on the plate is equivalent to that in the case of air moving pass a fixed flat plate with velocity u at large distances from the plate. Assuming that the air flow is laminar, the shear stress on one face of the plate can be calculated using Blasius solution for boundary layer [5], resulting in the following expression:

$$\tau_a = -\alpha_a \sqrt{\rho_a \mu_a} \sqrt{\frac{u^3}{x}}, \tag{A.54}$$

where $\rho_a = 1.2\,\mathrm{kg/m^3}$ and $\mu_a = 1.7 \times 10^{-5}\,\mathrm{kg/ms}$, respectively, are the density and viscosity of the ambient air. The constant $\alpha_a \approx 0.3$ can be calculated numerically from the Blasius boundary layer equation. We use the above expression in equation (2.2).

Although the air drag models presented here are rather simplistic, they capture the dynamics of flowing soap films. In chapter 2 we show that while the air drag is important, it does not play a crucial role in determining the jump in the film thickness. We adopt the Blasius model in our analysis of the soap-film equations because this model does not require any fitting parameters.

Appendix B

Friction factor data

Reynolds number	**Friction factor** ($\times 10^{-4}$)	**Width (mm)**
6300	3.96	5.2
6800	3.65	5.2
7600	4.08	6.2
9800	3.28	7.1
10000	3.88	7.3
10400	3.77	7.2
12100	3.35	7.1
13000	3.23	7.3
13200	3.25	7.1
14500	3.01	8.2
14800	3.34	7.2
15000	3.35	7.2
16500	3.05	8.2
19100	2.76	9.5
19300	2.86	9.5
20000	2.80	9.5
25600	2.86	12.7
26500	2.66	12.7
28100	2.43	13.5
31400	2.46	13.5
31500	2.74	13.5
31800	2.58	13.5
32600	2.77	13.5
38900	2.40	19.8
46700	2.41	21.0
50600	2.30	21.0

Table B.1: Friction factor in inverse energy cascade (taken by the author at Pittsburgh)

Reynolds number	**Friction factor** ($\times 10^{-4}$)	**Width (mm)**
3973	7.99	5.0
4441	7.61	5.0
5344	7.50	11.0
5419	7.15	11.0
5802	6.94	11.0
5803	7.54	11.0
6175	7.24	11.0
6786	6.74	11.0
7229	6.49	11.0
7893	6.41	11.0
9247	6.25	11.0
10631	5.89	11.0
11371	5.60	11.0
11656	5.79	11.0
12012	5.56	11.0
12131	6.00	11.0
12340	5.73	11.0
12706	5.00	11.0
13010	5.35	11.0
13170	5.04	11.0
13703	5.07	11.0
14034	4.61	11.0
14562	4.74	11.0
14605	4.77	11.0
15753	4.77	11.0
15825	4.65	11.0
16835	4.19	11.0
17463	4.46	11.0
17648	4.59	11.0
18202	4.19	11.0
19860	3.81	11.0
19913	4.19	11.0
21597	3.91	11.0
24013	3.64	11.0
25912	3.69	11.0
28963	3.66	17.0
30867	3.21	11.0
32029	3.75	17.0
37859	2.94	17.0
38996	3.07	26.0
46327	3.28	26.0

Table B.2: Friction factor in enstrophy cascade (taken by the author at Pittsburgh)

Reynolds number	**Friction factor** $(\times 10^{-4})$	**Width (mm)**
1320	16.53	12.0
1910	18.09	12.0
2418	12.14	12.0
3300	10.10	12.0
4800	7.81	12.0
5000	8.00	12.0
5400	8.49	12.0
9880	6.06	12.0
10680	6.31	12.0
19320	4.63	12.0
19800	4.82	12.0
22500	4.94	12.0
23210	3.46	12.0

Table B.3: Friction factor in enstrophy cascade (taken by Hamid Kellay at Bordeaux)

References

[1] G. Gioia and P. Chakraborty, "Turbulent friction in rough pipes and the energy spectrum of the phenomenological theory," *Physical Review Letters*, vol. 96, p. 044502, 2006.

[2] Y. Couder, J. Chomaz, and M. Rabaud, "On the hydrodynamics of soap films," *Physica D: Nonlinear Phenomena*, vol. 37, no. 1-3, pp. 384–405, 1989.

[3] K. Sreenivasan, "Fluid turbulence," *Reviews of Modern Physics*, vol. 71, no. 2, pp. 383–395, 1999.

[4] S. Pope and S. Pope, *Turbulent flows.* Cambridge University Press, 2000.

[5] H. Schlichting, K. Gersten, and K. Gersten, *Boundary-layer theory.* Springer, 2000.

[6] U. Frisch and A. Kolmogorov, *Turbulence: the legacy of AN Kolmogorov.* Cambridge University Press, 1995.

[7] A. N. Kolmogorov, "Local structure of turbulence in incompressible fluid at a very high reynolds number," *Dokl. Akad. Nauk. SSSR*, vol. 30, pp. 299–302, 1941. [English translation in Proc. R. Soc. London Ser. A 434 (1991)].

[8] A. Obukhov, "Energy distribution in the spectrum of turbulent flow," *Dokl. Akad. Nauk. SSSR*, vol. 32, pp. 22–24, 1941.

[9] J. Nikuradze, "Stromungsgesetze in rauhen Rohren," *VDI Forschungsheft*, vol. 361, no. 1, 1933. [English translation available as National Advisory Committee for Aeronautics, Tech. Memo. 1292 (1950). Online at: http://hdl.handle.net/2060/19930093938].

[10] J. Jiménez, "Turbulent flows over rough walls," *Annual Review of Fluid Mechanics*, vol. 36, no. 1, pp. 173–196, 2004.

[11] A. Chézy, "Memoire sur la vitesse de l'eau conduit dans une rigole donne," in *Dossier 847 (MS 1915)*, Ecole des Ponts et Chaussees, 1775. [English translation in Journal, Association of Engineering Societies, vol 18, 363–368, 1897].

[12] J. Dooge, "The manning formula in context," in *Channel flow resistance: centennial of Manning's formula* (B. C. Yen, ed.), pp. 136–185, Water Resoures Publications, Littleton, Colorado, 1992.

[13] B. Mckeon, C. Swanson, M. Zagarola, R. Donnelly, and A. Smits, "Friction factors for smooth pipe flow," *Journal of Fluid Mechanics*, vol. 511, pp. 41–44, 2004.

[14] M. Shockling, J. Allen, and A. Smits, "Roughness effects in turbulent pipe flow," *Journal of Fluid Mechanics*, vol. 564, pp. 267–285, 2006.

[15] J. Allen, M. Shockling, G. Kunkel, and A. Smits, "Turbulent flow in smooth and rough pipes," *Philosophical Transactions of the Royal Society A: Mathematical, Physical and Engineering Sciences*, vol. 365, no. 1852, p. 699, 2007.

[16] G. Kunkel, J. Allen, and A. Smits, "Further support for Townsend's Reynolds number similarity hypothesis in high Reynolds number rough-wall pipe flow," *Physics of Fluids*, vol. 19, p. 055109, 2007.

[17] L. Langelandsvik, G. Kunkel, and A. Smits, "Flow in a commercial steel pipe," *Journal of Fluid Mechanics*, vol. 595, pp. 323–339, 2008.

[18] S. Bailey, M. Hultmark, A. Smits, and M. Schultz, "Azimuthal structure of turbulence in high Reynolds number pipe flow," *Journal of Fluid Mechanics*, vol. 615, pp. 121–138, 2008.

[19] B. Mckeon, M. Zagarola, and A. Smits, "A new friction factor relationship for fully developed pipe flow," *Journal of Fluid Mechanics*, vol. 538, pp. 429–443, 2005.

[20] G. Barenblatt, "Scaling laws for fully developed turbulent shear flows. Part 1. Basic hypotheses and analysis," *Journal of Fluid Mechanics*, vol. 248, pp. 513–520, 1993.

[21] G. Barenblatt and A. Chorin, "A mathematical model for the scaling of turbulence," *Proceedings of the National Academy of Sciences*, vol. 101, no. 42, pp. 15023–15026, 2004.

[22] J. Lumley, "Drag reduction by additives," *Annual Review of Fluid Mechanics*, vol. 1, no. 1, pp. 367–384, 1969.

[23] P. Virk, "Drag reduction fundamentals," *AIChE Journal*, vol. 21, no. 4, pp. 625–656, 1975.

[24] C. White and M. Mungal, "Mechanics and prediction of turbulent drag reduction with polymer additives," *Annual Review of Fluid Mechanics*, vol. 40, pp. 235–256, 2008.

[25] T. Van Den Berg, S. Luther, and D. Lohse, "Energy spectra in microbubbly turbulence," *Physics of Fluids*, vol. 18, p. 038103, 2006.

[26] G. Gioia and F. Bombardelli, "Scaling and similarity in rough channel flows," *Physical Review Letters*, vol. 88, p. 014501, 2002.

[27] N. Guttenberg and N. Goldenfeld, "Friction factor of two-dimensional rough-boundary turbulent soap film flows," *Physical Review E*, vol. 79, no. 6, p. 65306, 2009.

[28] G. Gioia, P. Chakraborty, and F. A. Bombardelli, "Rough-pipe flows and the existence of fully developed turbulence," *Physics of Fluids*, vol. 18, p. 038107, 2006.

[29] M. Mehrafarin and N. Pourtolami, "Intermittency and rough-pipe turbulence," *Physical Review E*, vol. 77, p. 3, 2008.

[30] E. Calzetta, "Friction factor for turbulent flow in rough pipes from Heisenberg's closure hypothesis," *Physical Review E*, vol. 79, no. 5, p. 56311, 2009.

[31] G. Gioia and F. Bombardelli, "Localized turbulent flows on scouring granular beds," *Physical Review Letters*, vol. 95, no. 1, p. 14501, 2005.

[32] F. Bombardelli and G. Gioia, "Scouring of granular beds by jet-driven axisymmetric turbulent cauldrons," *Physics of fluids*, vol. 18, p. 088101, 2006.

[33] M. Rutgers, "Forced 2D turbulence: Experimental evidence of simultaneous inverse energy and forward enstrophy cascades," *Physical Review Letters*, vol. 81, no. 11, pp. 2244–2247, 1998.

[34] P. Tabeling, "Two-dimensional turbulence: a physicist approach," *Physics Reports*, vol. 362, no. 1, pp. 1–62, 2002.

[35] G. Batchelor, *The theory of homogeneous turbulence.* Cambridge University Press, 1982.

[36] H. Kellay and W. Goldburg, "Two-dimensional turbulence: a review of some recent experiments," *Reports on Progress in Physics*, vol. 65, p. 845, 2002.

[37] R. Kraichnan, "Inertial Ranges in Two-Dimensional Turbulence," *Physics of Fluids*, vol. 10, p. 1417, 1967.

[38] G. Batchelor, "Computation of the Energy Spectrum in Homogeneous Two-Dimensional Turbulence," *Physics of Fluids*, vol. 12, 1969.

[39] R. Kraichnan and D. Montgomery, "Two-dimensional turbulence," *Reports on Progress in Physics*, vol. 43, pp. 547–619, 1980.

[40] T. Tran, P. Chakraborty, G. Gioia, S. Steers, and W. Goldburg, "Marangoni shocks in unobstructed soap-film flows," *Physical Review Letters*, vol. 103, no. 10, p. 104501, 2009.

[41] T. Tran, P. Chakraborty, N. Guttenberg, A. Prescott, H. Kellay, W. Goldburg, N. Goldenfeld, and G. Gioia, "Macroscopic effects of the spectral structure in turbulent flows," *Nature Physics*, vol. 6, pp. 438–441, 2010.

[42] M. Gharib and P. Derango, "A liquid film (soap film) tunnel to study two-dimensional laminar and turbulent shear flows," *Physica D: Nonlinear Phenomena*, vol. 37, no. 1-3, pp. 406–416, 1989.

[43] M. Beizaie and M. Gharib, "Fundamentals of a liquid (soap) film tunnel," *Experiments in Fluids*, vol. 23, no. 2, pp. 130–140, 1997.

[44] J. Pedlosky, *Geophysical fluid dynamics.* Springer, 1987.

[45] C. Leith, "Atmospheric predictability and two-dimensional turbulence," *Journal of the Atmospheric Sciences*, vol. 28, no. 2, pp. 145–161, 1971.

[46] C. Leith and R. Kraichnan, "Predictability of turbulent flows," *Journal of the Atmospheric Sciences*, vol. 29, no. 6, pp. 1041–1058, 1972.

[47] M. Lesieur, *Turbulence in fluids.* Springer, 2008.

[48] P. Marcus, "Prediction of a global climate change on Jupiter," *Nature*, vol. 428, no. 6985, pp. 828–831, 2004.

[49] F. Seychelles, Y. Amarouchene, M. Bessafi, and H. Kellay, "Thermal Convection and Emergence of Isolated Vortices in Soap Bubbles," *Physical Review Letters*, vol. 100, no. 14, p. 144501, 2008.

[50] M. Rutgers, X. Wu, and W. Daniel, "Conducting fluid dynamics experiments with vertically falling soap films," *Review of Scientific Instruments*, vol. 72, p. 3025, 2001.

[51] D. Georgiev and P. Vorobieff, "The slowest soap-film tunnel in the Southwest," *Review of Scientific Instruments*, vol. 73, p. 1177, 2002.

[52] M. Rutgers, R. Bhagavatula, A. Petersen, and W. Goldburg, "Two-dimensional velocity profiles and laminar boundary layers in flowing soap films," *Physics of Fluids*, vol. 8, p. 2847, 1996.

[53] C. Wen, S. Chang-Jian, and M. Chuang, "Analogy between soap film and gas dynamics. II. Experiments on one-dimensional motion of shock waves in soap films," *Experiments in Fluids*, vol. 34, no. 2, pp. 173–180, 2003.

[54] T. Faber, *Fluid dynamics for physicists.* Cambridge University Press, 1995.

[55] D. Bonn, A. Andersen, and T. Bohr, "Hydraulic jumps in a channel," *Journal of Fluid Mechanics*, vol. 618, pp. 71–87, 2008.

[56] C. Navier, "Mémoire sur les lois du mouvement des fluides," *Mém. Acad. Sci. Inst. France*, vol. 6, no. 2, pp. 375–394, 1822.

[57] G. Stokes, "On the theories of the internal friction of fluids in motion, and of the equilibrium and motion of elastic solids," *Transactions of the Cambridge Philosophical Society*, vol. 8, no. 2, p. 287, 1845.

[58] O. Reynolds, "An experimental investigation of the circumstances which determine whether the motion of water shall be direct or sinuous, and of the law of resistance in parallel channels," *Philosophical Transactions of the Royal Society of London*, vol. 174, pp. 935–982, 1883.

[59] H. Blasius, "Das Ähnlichkeitsgesetz bei Reibungsvorgängen in Flüssigkeiten," *Forschg. Arb. Ing.-Wes*, vol. 134, 1913.

[60] L. Prandtl, *Essentials of fluid dynamics.* Hafner Publishing Company, 1952.

[61] A. Strickler, "Beitrage zur frage der geschwindigkeitsformel und der rauhigkeitszahlen fur strome, kanale und geschlossene leitungen." Mitteilungen des Eidgenössischen Amtes für Wasserwirtschaft 16, Bern, Switzerland. Translated as "Contributions to the question of a velocity formula and roughness data for streams, channels and closed pipelines." by T. Roesgan and W. R. Brownie, Translation T-10, W. M. Keck Lab of Hydraulics and Water Resources, Calif. Inst. Tech., Pasadena, Calif. January 1981, 1923.

[62] L. Richardson, "Atmospheric diffusion shown on a distance-neighbour graph," *Proceedings of the Royal Society of London. Series A, Containing Papers of a Mathematical and Physical Character*, vol. 110, no. 756, pp. 709–737, 1926.

[63] D. Tritton, *Physical Fluid Dynamics.* Oxford Science Publications, 1988.

[64] G. Taylor, "The spectrum of turbulence," *Proceedings of the Royal Society of London. Series A, Mathematical and Physical Sciences*, vol. 164, no. 919, pp. 476–490, 1938.

[65] A. Belmonte, B. Martin, and W. Goldburg, "Experimental study of Taylor's hypothesis in a turbulent soap film," *Physics of Fluids*, vol. 12, no. 4, pp. 835–845, 2000.

[66] H. Kellay, X. Wu, and W. Goldburg, "Experiments with turbulent soap films," *Physical Review Letters*, vol. 74, no. 20, pp. 3975–3978, 1995.

[67] K. Mysels, S. Frankel, and K. Shinoda, *Soap films: studies of their thinning and a bibliography.* Pergamon Press, 1959.

[68] C. Isenberg, *The science of soap films and soap bubbles.* Dover Publications, 1992.

[69] Y. Couder, "Two-dimensional grid turbulence in liquid film," *Journal de Physique Lettres*, vol. 45, pp. 353–366, 1984.

[70] O. Cardoso, D. Marteau, and P. Tabeling, "Quantitative experimental study of the free decay of quasi-two-dimensional turbulence," *Physical Review E*, vol. 49, no. 1, pp. 454–461, 1994.

[71] P. Tabeling, S. Burkhart, O. Cardoso, and H. Willaime, "Experimental study of freely decaying two-dimensional turbulence," *Physical Review Letters*, vol. 67, no. 27, pp. 3772–3775, 1991.

[72] J. Paret and P. Tabeling, "Intermittency in the two-dimensional inverse cascade of energy: Experimental observations," *Physics of Fluids*, vol. 10, p. 3126, 1998.

[73] M. Rivera and X. Wu, "External dissipation in driven two-dimensional turbulence," *Physical Review Letters*, vol. 85, no. 5, pp. 976–979, 2000.

[74] J. Sommeria, "Experimental study of the two-dimensional inverse energy cascade in a square box," *Journal of Fluid Mechanics*, vol. 170, pp. 139–168, 2006.

[75] C. Tropea, A. Yarin, and J. Foss, *Springer handbook of experimental fluid mechanics*. Springer, 2007.